

Atmospheric circulation of brown dwarfs and directly imaged exoplanets driven by cloud radiative feedback: effects of rotation

Xianyu Tan¹★ and Adam P. Showman^{2,3,†}

¹*Atmospheric, Oceanic and Planetary Physics, Department of Physics, University of Oxford, OX1 3PU, UK*

²*Lunar and Planetary Laboratory, University of Arizona, 1629 University Boulevard, Tucson, AZ 85721, USA*

³*Department of Atmospheric and Oceanic Sciences, Peking University, Beijing, People's Republic of China*

† Deceased.

Accepted XXX. Received YYY; in original form ZZZ

ABSTRACT

Observations of brown dwarfs (BDs), free-floating planetary-mass objects and directly imaged extrasolar giant planets (EGPs) exhibit rich evidence of large-scale weather. Cloud radiative feedback has been proposed as a potential mechanism driving the vigorous atmospheric circulation on BDs and directly imaged EGPs, and yet it has not been demonstrated in three-dimensional (3D) dynamical models at relevant conditions. Here we present a series of atmospheric circulation models that self-consistently couple dynamics with idealized cloud formation and its radiative effects. We demonstrate that vigorous atmospheric circulation can be triggered and self-maintained by cloud radiative feedback. Typical isobaric temperature variation could reach over 100 K and horizontally averaged wind speed could be several hundred m s^{-1} . The circulation is dominated by cloud-forming and clear-sky vortices that evolve over timescales from several to tens of hours. The typical horizontal lengthscale of dominant vortices is closed to the Rossby deformation radius, showing a linear dependence on the inverse of rotation rate. Stronger rotation tends to weaken vertical transport of vapor and clouds, leading to overall thinner clouds. Domain-mean outgoing radiative flux exhibits variability over timescales of tens of hours due to the statistical evolution of storms. Different bottom boundary conditions in the models could lead to qualitatively different circulation near the observable layer. The circulation driven by cloud radiative feedback represents a robust mechanism generating significant surface inhomogeneity as well as irregular flux time variability. Our results have important implications for near-IR colors of dusty BDs and EGPs, including the scatter in the near-IR color-magnitude diagram and the viewing-geometry dependent near-IR colors.

Key words: hydrodynamics — methods: numerical — planets and satellites: atmospheres — planets and satellites: gaseous planets — brown dwarfs

1 INTRODUCTION

Active weather is likely common among brown dwarfs (BDs) as has been indicated by several lines of evidence. First, atmospheric circulation drives temperature anomalies and inhomogeneous cloud coverage on a global scale, which is likely responsible for the observed lightcurve variability of many L and T dwarfs (e.g., Artigau et al. 2009; Radigan et al. 2012; Buenzli et al. 2012; Apai et al. 2013; Buenzli et al. 2014; Wilson et al. 2014; Metchev et al. 2015; Yang et al. 2016; Leggett et al. 2016b; Miles-Páez et al. 2017; Apai et al. 2017; Manjavacas et al. 2017; Zhou et al. 2018; Vos et al. 2019; Eriksson et al. 2019; Lew et al. 2020; Zhou et al. 2020; Bowler et al. 2020; Hitchcock et al. 2020; Vos et al. 2020, see also recent reviews by Biller 2017 and Artigau 2018). Second, spectra and near-IR colors of many L dwarfs suggest the presence of thick clouds in their photospheres (e.g., Chabrier et al. 2000; Allard et al. 2001; Tsuji 2002; Burrows et al. 2006; Saumon & Marley 2008; Charnay et al. 2018). The existence of thick clouds indicates the presence of atmospheric dynamics against gravitational settling. Third, the abrupt transition

from L to T dwarfs is likely caused by either a sudden change of cloud patchiness or thickness (Ackerman & Marley 2001; Burgasser et al. 2002; Knapp et al. 2004; Marley et al. 2010), for which atmospheric dynamics likely plays a role. Fourth, large-scale circulation provides a source of vertical mixing that helps to explain the inferred chemical disequilibrium in a wide range of BDs (e.g., Saumon et al. 2006; Stephens et al. 2009; Leggett et al. 2016a, 2019; Miles et al. 2020), especially in stratified atmospheres where convection does not play a direct role in mixing. Other techniques detecting or constraining the presence of global circulation of BDs include Doppler imaging (Crossfield et al. 2014), simultaneous tracking of near-IR and radio variability (Allers et al. 2020) and precise near-IR polarization measurements (Millar-Blanchaer et al. 2020).

Extrasolar giant planets (EGPs) detected by the direct imaging technique so far are mostly young, hot and relatively distant from their host stars, and therefore they receive negligible stellar bolometric flux compared to their internal heat flux. Their atmospheric structure and dynamics are likely determined mostly by internal luminosity, and thus they fall into the same category as field BDs in terms of atmospheric characteristics. Similar to BDs, the near-IR spectrum and color of most directly imaged EGPs suggest the pres-

* E-mail: xianyu.tan@physics.ox.ac.uk

ence of thick clouds and possibly significant chemical disequilibrium in their photospheres (e.g., Currie et al. 2011; Barman et al. 2011a,b; Marley et al. 2012; Oppenheimer et al. 2013; Ingraham et al. 2014; Rajan et al. 2015; Moses et al. 2016; Chauvin et al. 2017; Stolker et al. 2020). Although current instruments place a high threshold for the detection of lightcurve variability of directly imaged EGPs orbiting bright stars¹, their planetary-mass, free-floating counterparts commonly exhibit lightcurve variability (Biller et al. 2015; Zhou et al. 2016; Vos et al. 2018; Biller et al. 2018; Schneider et al. 2018; Manjavacas et al. 2019; Miles-Páez et al. 2019).

Understanding the atmospheric circulation of BDs and directly imaged EGPs is a pressing need given the large body of observational constraints. Unlike planets in close-to-modest distances from their host stars whose atmospheric circulation is primarily driven by the horizontal differential stellar irradiation, atmospheres of relatively isolated BDs and directly imaged EGPs lack horizontal differential heating from external sources, and their atmospheric circulation is driven almost solely by internal heat flux. So far, two major categories of sources have been proposed to drive the global circulation in the stratified, observable atmospheric layers.

The first is a mechanically forced scenario: convection interacts with the overlying stratified atmospheres and generates a wealth of waves and turbulence. These atmospheric eddies interact with the large-scale flows, driving large-scale circulation. There have been a few studies in this direction. Local hydrodynamic simulations by Freytag et al. (2010) show that gravity waves generated by interactions between the convective interior and the stratified layer can cause mixing and lead to small-scale cloud patchiness. Showman & Kaspi (2013) presented global convection models and analytically estimated typical wind speed and horizontal temperature differences driven by the absorption and breaking of atmospheric waves in the stably stratified atmosphere. By injecting random forcing to a shallow-water system, Zhang & Showman (2014) showed that weak radiative dissipation and strong forcing favor large-scale zonal jets for BDs, whereas strong dissipation and weak forcing favor transient eddies and quasi-isotropic turbulence. Using a general circulation model coupled with parameterized thermal perturbations resulting from interactions between convective interior and the stratified atmosphere, Showman et al. (2019) showed that under conditions of relatively strong forcing and weak damping, robust zonal jets and the associated meridional circulation and temperature structure are common outcomes of the dynamics. They also demonstrated that long-term (multi months to years) quasi-periodic oscillations on the equatorial zonal jets, similar to the Quasi-biennial oscillation observed in Earth’s stratosphere, can be driven by the thermal perturbations.

The second scenario is a thermally-driven mechanism linked to cloud radiative feedback (Tan & Showman 2019). Clouds are critical in shaping the thermal structure, near-IR color and spectral properties of substellar atmospheres via large opacity loading (see recent reviews by Helling & Casewell 2014, Marley & Robinson 2015 and Helling 2019). Cloud radiative feedback is similarly important in driving a vigorous global circulation and atmospheric variability.

¹ Detecting variability of directly imaged exoplanets requires precisely removing contamination from the point spread function of the bright hot star. The current state-of-the-art ground based extreme adaptive optics observations can reach ~10% precision in high-cadence time series (Apai et al. 2016). Typical amplitudes of rotational modulations are much smaller than this level (Artigau 2018). Additional limitations may arise if the viewing angle of the exoplanets is close to polar view (and therefore the rotational modulation is minimized), or due to stellar variability.

Imagine an atmosphere consisted of patchy clouds. In the cloudy region, less thermal radiation escapes to space from to top of the cloud where it is relatively cold, whereas, in the cloudless region, more radiation to space occurs from much deeper and hotter regions. The two regions will, therefore, experience extremely different vertical profiles of radiative heating and cooling, which will lead to horizontal temperature differences on isobars. These horizontal temperature contrasts will drive an overturning circulation that, in turn, can advect cloud condensate vertically, and in principle might be capable of maintaining the cloud patchiness.

There are two distinct cloud radiative feedbacks. The first one involves interactions between cloud formation, cloud radiative feedback and small-scale convective transport of tracers. It can result in spontaneous variability of both the cloud and thermal structures locally in an atmospheric column that occupies a small horizontal area. This has been extensively demonstrated in Tan & Showman (2019) using a simple one-dimensional (1D), time-dependent model that couples radiative transfer, cloud formation, and small-scale convective mixing. In a large-scale sense, this generation of spontaneous variability is intrinsically 1D, without requirement of explicit 3D large-scale flows. The second feedback with the large-scale circulation requires intrinsically multi-dimensional flows. When clouds are advected by large-scale motions, and the large-scale motions are driven by the radiative heating or cooling associated with cloud properties, such a system could be linearly unstable, providing an energy source to drive the circulation (Gierasch et al. 1973).

The latter multi-dimensional cloud radiative feedback has never been investigated for giant planets in the fully nonlinear regime. There is a strong motivation to examine this cloud feedback in a full numerical model and explore its dynamical properties. In reality, this form of feedback cloud be important in atmospheres of many BDs and directly imaged EGPs, for example, for some L dwarfs or late T dwarfs in which clouds condense in the upper stratified atmospheres where convection does not directly provide mixing (e.g., Tsuji 2002; Burrows et al. 2006; Morley et al. 2012). In this situation, the intrinsic 1D variability driven by cloud feedback would not occur. The evolution of clouds and temperature anomalies would rely on the explicit large-scale flows.

In this study, we numerically investigate effects of the cloud radiative feedback on driving a large-scale circulation in the context of BDs and directly imaged EGPs using idealized general circulation models that couple cloud formation and their radiative feedbacks to the flows. We tune the model parameters such that clouds form in the stratified layers and the 1D intrinsic variability would not occur, leaving us a clean environment to understand the multi-dimensional cloud radiative feedback. We emphasize that this study does not directly aim at addressing the role of dynamics on the L/T transition, but to illustrate the fundamental dynamical properties of cloudy atmospheres relevant to those of dusty L dwarfs.

We have three basic conclusions from this study: 1) vigorous atmospheric circulation can be triggered and self-sustained by the cloud radiative feedback, providing a mechanism for surface inhomogeneous and its short-term evolution for BDs and directly imaged EGPs; 2) typical horizontal lengthscales of storms are closely related to the Rossby deformation radius, which is inversely proportional to the local rotational rate when other parameters are the same; 3) the vertical extent of clouds decreases with increasing rotation rate.

This paper is organized as follows. Section 2 introduces the numerical model. Section 3 describes results from models with varying Coriolis parameters f . In section 4 we discuss our results and implications, then finally draw conclusions in section 5.

2 GENERAL CIRCULATION MODEL

We solve the standard 3D hydrostatic primitive equations in pressure coordinates. These are standard dynamical equations used in dynamical meteorology for a stratified atmosphere with horizontal lengthscales that greatly exceed vertical lengthscales (for a review, see Vallis 2006), as appropriate to the global-scale atmospheric flows in photospheres of BDs and giant planets. Two tracer equations representing condensible vapor and clouds are simultaneously integrated. The horizontal momentum, hydrostatic equilibrium, continuity, thermodynamic, and tracer equations governing condensible vapor and clouds are as follows, respectively,

$$\frac{d\mathbf{v}}{dt} = -f\hat{k} \times \mathbf{v} - \nabla_p \Phi + \mathcal{R}_v, \quad (1)$$

$$\frac{\partial \Phi}{\partial p} = -\frac{1}{\rho}, \quad (2)$$

$$\nabla_p \cdot \mathbf{v} + \frac{\partial \omega}{\partial p} = 0, \quad (3)$$

$$\frac{d\theta}{dt} = \frac{g\theta}{c_p T} \frac{\partial F}{\partial p} + \mathcal{R}_\theta, \quad (4)$$

$$\frac{dq_v}{dt} = -\delta \frac{q_v - q_s}{\tau_c} + (1 - \delta) \frac{\min(q_s - q_v, q_c)}{\tau_c} + Q_{\text{deep}}, \quad (5)$$

$$\frac{dq_c}{dt} = \delta \frac{q_v - q_s}{\tau_c} - (1 - \delta) \frac{\min(q_s - q_v, q_c)}{\tau_c} - \frac{\partial(q_c V_s)}{\partial p}, \quad (6)$$

where \mathbf{v} is the horizontal velocity vector on isobars, $\omega = dp/dt$ is the vertical velocity in pressure coordinates, f is the Coriolis parameter, Φ is the geopotential, \hat{k} is the local unit vector in the vertical direction, ρ is the gas density, ∇_p is the horizontal gradient in pressure coordinate, $d/dt = \partial/\partial t + \mathbf{v} \cdot \nabla_p + \omega \partial/\partial p$ is the material derivative, $\theta = T(p_0/p)^{R/c_p}$ is the potential temperature, $p_0 = 1$ bar is a reference pressure, R is the specific gas constant and c_p is the specific heat at constant pressure. The ideal gas law $p = \rho RT$ is used for the equation of state for the atmosphere.

\mathcal{R}_v represents a Rayleigh frictional drag applied to horizontal winds in the deep layers of our models to crudely represent the effects of momentum mixing between the weather layer and the quiescent interior (which is deeper than our simulation domain) where large-scale flows are likely to be retarded due to significant magnetohydrodynamic dissipation. Given the rapid convective mixing of specific entropy in the convective region and the fast rotation of BDs, the Taylor–Proudman effect may be efficient in slowing down large-scale winds in the shallow layer (see the detailed argument in Schneider & Liu 2009). Because of the much hotter interior of L and T dwarfs and likely strong magnetic fields, the conducting region in BDs is expected to extend to a much shallower depth than that of Jupiter. Therefore this “drag” effect is applied uniformly in our study. The drag linearly decreases with decreasing pressure: $\mathcal{R}_v = -k_v(p)\mathbf{v}$, where $k_v(p)$ is a pressure-dependent drag coefficient, which decreases from $1/\tau_{\text{drag}}$ (where τ_{drag} is a characteristic drag timescale) at the bottom pressure boundary p_{bot} to zero at certain pressure $p_{\text{drag,top}}$:

$$k_v(p) = \frac{1}{\tau_{\text{drag}}} \max\left(0, \frac{p - p_{\text{drag,top}}}{p_{\text{bot}} - p_{\text{drag,top}}}\right). \quad (7)$$

Note that this form of drag has been used in previous studies of hot Jupiters (e.g., Liu & Showman 2013; Tan & Komacek 2019;

Carone et al. 2020). The strength of this drag could influence the qualitative dynamics in the cloud-forming region as will be shown in Section 3.4. In all simulations, we fix $p_{\text{drag,top}}$ to 5 bars, which is much deeper than cloud forming regions and does not directly affect cloud formation. Kinetic energy dissipated by the frictional drag is converted to thermal heating by the term \mathcal{R}_θ . Due to the unknown nature of interactions between the interior and the weather layer in BDs and EGPs, the characteristic drag timescale τ_{drag} is treated as a free parameter to explore possible circulation patterns. For major sets of simulations presented below, we adopt $\tau_{\text{drag}} = 10^5$ s. We assume that the temperature at the model bottom boundary remains fixed during evolution, mimicking an atmosphere attached to a convective interior with a specific entropy that does not evolve over short timescales.

The deep layers of our models reach the convectively unstable region. We parameterize effects of rapid convective mixing using a simple convective adjustment scheme as in the NCAR Community Atmosphere Model (Collins et al. 2004, see their Section 4.6). If any adjacent two layers within a vertical atmospheric column are unstable, they are instantaneously adjusted to a convectively neutral state while conserving total sensible heat $\sum \Delta p T$, where Δp is the layer thickness in pressure. In a single dynamical step, the whole column is repeatedly scanned until convective instability is eliminated everywhere. Tracers are also well homogenized within the adjusted domain during adjustment. There is no adjustment in the horizontal direction.

As in Tan & Showman (2019), in calculating the net thermal radiative flux F we assume a grey atmosphere (with a single broad thermal band) in a plane-parallel, two-stream, multiple-scattering approximation. The radiative transfer equations in an absorbing, emitting and multiple scattering media with the δ -function adjustment for scattering are solved using the efficient numeral package TWOSTR (Kylling et al. 1995, their equations (7) and (8) are solved in our model.). The background model atmosphere uses a frequency-averaged gas opacity, the Rosseland-mean opacity $\kappa_{R,g}$, from Freedman et al. (2014) with solar composition. The Rosseland-mean opacity gives a good estimation of radiative fluxes in the optically thick limit. In this study, clouds can extend to the upper atmosphere where it is optically thin by the gas opacity alone. In these regions there is no good choice *a priori* for a single opacity in the grey approximation. Therefore, we impose a constant minimal opacity κ_{min} in the whole atmosphere, such that the gaseous opacity is $\kappa_{\text{gas}} = \max(\kappa_{R,g}, \kappa_{\text{min}})$. In most of the cases we chose $\kappa_{\text{min}} = 10^{-3} \text{ m}^2 \text{ kg}^{-1}$.² This value has been used previously for the thermal opacity of typical hot Jupiter’s atmospheres (Guillot 2010) whose atmospheric temperatures are close to those of BDs. The total atmospheric opacity κ is simply the sum of the gas and cloud opacities $\kappa = \kappa_{\text{gas}} + \kappa_c$, the latter being determined by instantaneous cloud mixing ratio as a function of time and location as will be described below.

² We have tested additional models with $\kappa_{\text{min}} = 0$, $\kappa_{\text{min}} = 10^{-4}$, and $\kappa_{\text{min}} = 10^{-2} \text{ m}^2 \text{ kg}^{-1}$. The resulting typical circulation pattern, mean temperature structure and outgoing thermal flux are qualitatively very similar among cases with $\kappa_{\text{min}} = 0$, $\kappa_{\text{min}} = 10^{-4}$ and $\kappa_{\text{min}} = 10^{-3} \text{ m}^2 \text{ kg}^{-1}$. This is expected because when $\kappa_{\text{min}} \lesssim 10^{-3} \text{ m}^2 \text{ kg}^{-1}$, the overall thermal structure is determined by the combination of the cloud opacity and the Rosseland-mean gas opacity. Cloud opacity usually dominates over the gas opacity, which is why clouds can drive circulation. The case with $\kappa_{\text{min}} = 10^{-2} \text{ m}^2 \text{ kg}^{-1}$ exhibits a slightly different mean thermal structure because κ_{min} is large enough to affect the overall temperature-pressure profile even without the cloud opacity. We concluded that as long as $\kappa_{\text{min}} \ll 10^{-2} \text{ m}^2 \text{ kg}^{-1}$ our results are not sensitive to the choice of κ_{min} .

q_v is the mass mixing ratio of condensable vapor relative to the dry background air and q_c is the mass mixing ratio of cloud particles. The terms $\delta(q_v - q_s)/\tau_c$ and $(1 - \delta)\min(q_s - q_v, q_c)/\tau_c$ are sources/sinks due to condensation and evaporation, respectively. q_s is the local saturation vapor mixing ratio and τ_c is a conversion timescale between vapor and condensates. We set $\delta = 1$ when vapor is supersaturated and $\delta = 0$ otherwise. The conversion timescale τ_c is very short compared to dynamical timescales in conditions relevant to BDs and EGP (Helling & Casewell 2014), and here we set $\tau_c = 10^2$ s which is slightly longer than a dynamical time step for numerical stability. Cloud and dust formation in substellar atmospheres is highly complex (see reviews by, for example, Helling & Fomins 2013; Helling 2019), and many models adopt the idealized, chemical equilibrium framework (see summaries in Ackerman & Marley 2001; Helling et al. 2008; Marley & Robinson 2015). Here we adopt an even more simplified approach—the saturation vapor mixing ratio q_s is assumed to depend on pressure alone. In this way, dynamical cloud properties (horizontal lengthscale and vertical extent of clouds) depend on dynamics alone (more specifically, rotation). We specify a uniform pressure p_{cond} , lower than which q_s decreases with decreasing pressure and higher than which q_s is arbitrarily large such that no condensation would occur:

$$\begin{cases} q_s = q_{\text{deep}}(p/p_{\text{cond}})^3 & (p \leq p_{\text{cond}}), \\ q_s = \infty & (p > p_{\text{cond}}), \end{cases} \quad (8)$$

where q_{deep} is the deep vapor mixing ratio. In this study p_{cond} is assumed to be 0.5 bar, and q_{deep} is assumed to be equal to 2×10^{-4} kg/kg. Both choices are turned to satisfy conditions that convection is absent in the cloud forming regions while maintaining a vigorous circulation. The power law exponent of 3 in Equation (8) is chosen non-rigorously: as long as q_s sharply decrease with decreasing pressure, the resulting cloud formation is representative enough for the purpose of investigating dynamics. We have tested additional models with power law exponents of 5 and 7, and they show qualitatively similar results. The term $Q_{\text{deep}} = -(q_v - q_{\text{deep}})/\tau_{\text{deep}}$ represents replenishment of condensable vapor by deep convection over a characteristic timescale τ_{deep} , which is applied only at pressure deeper than 5 bars. τ_{deep} is generally set to 10^3 s, broadly consistent with mixing timescales over a pressure scale height near the upper convective zone (Showman & Kaspi 2013).

We assume a constant cloud particle number per dry air mass N_c (in unit of kg^{-1}) throughout the atmosphere, then use N_c to determine local cloud particle size with given time- and location-dependent amount of condensate q_c . Cloud particles are assumed to have a single size locally in each grid cell, and the particle size r_c is then determined via

$$r_c = \left(\frac{3q_c}{4\pi N_c \rho_c} \right)^{1/3}, \quad (9)$$

where ρ_c is the density of condensate. Radiation interacts with cloud particles by absorption and scattering, which we parameterize by the extinction coefficient Q_{ext} , scattering coefficient Q_{scat} and asymmetry parameter \bar{g} . As in Tan & Showman (2019), the total cloud extinction opacity given a particle size $\kappa_c(r_c)$ is obtained by averaging over all wavelengths λ using the Rosseland-mean definition:

$$\frac{1}{\kappa_c(r_c)} = \frac{\int_0^\infty \frac{1}{\kappa_{\text{ext}}(\lambda)} \frac{dB_\lambda}{dT} d\lambda}{\int_0^\infty \frac{dB_\lambda}{dT} d\lambda}, \quad (10)$$

where B_λ is the Planck function and $\kappa_{\text{ext}}(\lambda) = N_c \pi r_c^2 Q_{\text{ext}}(r_c, \lambda)$ is

the cloud opacity at λ . Assuming spherical particles, the Rosseland-mean Q_{ext} , Q_{scat} and \bar{g} as a function of temperature and particle size are calculated with Mie theory using the numerical package developed by Schäfer et al. (2012)³. We pre-calculate tables containing these parameters as functions of temperature and pressure, and read them into the GCM using linear interpolation during the simulations. In this study, we use enstatite (MgSiO_3) to represent properties of the cloud species, including a density $\rho_c = 3190 \text{ kg m}^{-3}$ and the refractive index of enstatite obtained from Jäger et al. (2003). The results are not sensitive to the choice of cloud species because the essence of clouds is generating radiative heating/cooling that drives the dynamics. In all simulations we assume $N_c = 10^{11} \text{ kg}^{-1}$, which means with the specified deep vapor abundance the condensed particle size is around $0.5 \mu\text{m}$, consistent with the expected sub-micron particles in L dwarfs (Burningham et al. 2017). With a given particle size, the cloud settling velocity V_s as a function of pressure and temperature is calculated using Eqs. (3)-(7) of Parmentier et al. (2013).

Our models assume a Cartesian geometry, periodic horizontal boundary conditions and a constant Coriolis parameter f across the whole model domain—the so-called f -plane approximation. BDs are likely rapid rotators. Doppler broadening of spectral lines (Reiners & Basri 2008) and rotation periods inferred from lightcurve variability (e.g., Artigau et al. 2009; Radigan et al. 2012; Metchev et al. 2015; Apai et al. 2017; Allers et al. 2020) indicate typical rotation period of less than two hours to slightly more than 10 hours for field BDs. Planetary-mass, free-floating giant planets and Directly imaged EGPs likely rotate rapidly as well (Snellen et al. 2014; Zhou et al. 2016; Bryan et al. 2018). From equator to pole, atmospheric dynamics of BDs and directly imaged EGPs is likely affected by a wide range of local f , and the key dynamical lengthscales that are closely linked to the local planetary rotation may vary substantially. Therefore, f will be systematically varied while keeping other parameters the same in our models to thoroughly investigate effects of rotation on the circulation driven by cloud radiative feedback.

The reason we start our investigations with a f -plane approximation instead of full global models is the following. Turbulence is horizontally homogeneous under the constant- f assumption, which is considerably simpler than that in the full spherical geometry in which the latitudinal-dependent f induces horizontal anisotropy in the turbulence (Rhines 1975; Vallis & Maltrud 1993). This strategy provides a clearer context to explore effects of varying rotation on turbulence and cloud formation. Indeed, in a long history of investigations of geophysical turbulence (e.g., De Verdiere 1980; McWILLIAMS et al. 1999; Arbic & Flierl 2003; Arbic et al. 2007) and Earth's tropical cyclones (e.g., Held & Zhao 2008; Zhou et al. 2014), theories and models using the f -plane assumption have yielded significant insights on the properties of turbulence before considering a spherical geometry. Dynamics in global models will be investigated in a further study.

The dynamical equations (Equations 1-6) are solved using an atmospheric general circulation model, the MITgcm (Adcroft et al. 2004, see also mitgcm.org). A standard fourth-order Shapiro filter is applied in the horizontal velocity and temperature fields to maintain numerical stability (Shapiro 1970), which smooths out grid-scale variations but has minimal effect on the large-scale structure. We assume periodic horizontal boundary conditions. For most models presented below, we assume a horizontal domain size of 3×10^4 km. The resulting area is relatively small compared to the planetary surface assuming a Jupiter sized object such that the constant f ap-

³ <https://uk.mathworks.com/matlabcentral/fileexchange/36831-matscat>

proximation holds, while remaining large enough to ensure proper statistical analysis in some cases. The pressure domain is between 10 bars and 10^{-3} bar, which is discretized evenly into 55 layers in log pressure. Temperature at the bottom boundary (10 bars) is fixed at 2600 K. Under cloud free conditions, the resulting effective temperature is ~ 1700 K. With clouds, as will be shown in Section 3, the effective temperature is ~ 1500 K, which is appropriate for typical mid-to-late L dwarfs (e.g., Kirkpatrick et al. 2012). For the major models shown below, horizontal resolution is 150 km or 100 km per grid cell depending on f , which is sufficient to fully resolve dynamics within a Rossby deformation radius⁴. The dynamical time step is typically 30 s. We adopt physical parameters relevant for BDs, including the specific heat $c_p = 1.3 \times 10^4 \text{ J kg}^{-1} \text{ K}^{-1}$, specific gas constant $R = 3714 \text{ J kg}^{-1} \text{ K}^{-1}$, and surface gravity $g = 1000 \text{ ms}^{-2}$.

Our models do not include an upper sponge layer which is typically used to minimize effects of wave reflection from the upper boundary on dynamics at levels of interest. We have performed additional tests for models with and without the sponge layer, and found that weather including the sponge layer or not do not affect the quantitative dynamical properties associated with cloud radiative feedback. These tests are shown in the supplemental document (numerical_test.pdf) associated with this paper. In addition, we have performed a sensitivity test of horizontal resolution on a 3D model with $f = 4 \times 10^{-4} \text{ s}^{-1}$. Statistical results of the test show good convergence, suggesting that our current horizontal resolution is adequate to capture the essential dynamics. The resolution test is also contained in the supplemental document (numerical_test.pdf). We have tested additional models with different Shapiro filter timescales with either a third-order or fourth-order filter (note that the fourth-order filter which is the weaker one is used in our study). Those results are quantitatively similar, including the mean cloud mixing ratio and kinetic energy spectrum. Therefore, the physical phenomenon seen in our results and conclusions of this study should be independent of numerical setup of the numerical diffusion.

3 RESULTS

3.1 Non-rotating two-dimensional dynamics

3.1.1 Cloud radiative instability and initial evolution

The concept of cloud radiative instability which was first introduced by Gierasch et al. (1973) is particularly relevant in the cloud-driven circulation of BDs and directly imaged EGPs. Large-scale dynamical instability may occur when the radiative heating depends on cloud properties, and when cloud properties depend on the large-scale vertical motion driven by the radiative heating rate. The essence of this instability can be illustrated using a simple linearized thermodynamic system as described in Gierasch et al. (1973). Let's assume that clouds are optically thick and that the atmospheric column was originally at rest and radiative equilibrium. The change of outgoing thermal flux could be due to brightness temperature deviations that are caused by either actual temperature variation or the cloud-top altitude variation. A slight perturbation of cloud-top altitude results in a change in the outgoing thermal flux. Let's suppose that the

perturbation moves the cloud top upward to a colder altitude. The outgoing thermal flux decreases, and the atmospheric column is then no longer in equilibrium and radiative heating occurs. Large-scale vertical upwelling occurs in response to the heating, advecting the cloud top further upward (here the cloud settling speed is assumed to be smaller than the flow vertical velocity). This causes even less thermal flux emitted to space, which induces stronger heating and ascending, providing a positive feedback to the system.

Gierasch's theory predicts an initial growth rate $\sim \Gamma_c / (\bar{\Gamma} \tau)$ for the vertical velocity, where $\tau = \frac{c_p M}{4\sigma T_c^3}$ represents a radiative timescale, σ is the Stefan-Boltzmann constant, T_c is cloud-top temperature, M is atmospheric column mass, $\Gamma_c = |dT_c/dz|$, T_c is the cloud-top temperature, and $\bar{\Gamma} = \frac{d\bar{T}}{dz} + \frac{g}{c_p}$.

Gierasch et al. (1973) further showed that unstable linear modes are possible when the cloud radiative instability is coupled to the linearized dynamical systems. In the absence of rotation, 2D hydrostatic gravity waves have a set of pure unstable growing modes (no propagation) and sets of attenuating, eastward and westward propagating modes.

The linear model of Gierasch et al. (1973) serves as a valuable starting point. To better appreciate the transition from an initially linear to a nonlinear state, we start off our numerical investigation with an initial value problem. The simplest setup is a two-dimensional (2D) model in length-pressure domain with a periodic horizontal boundary condition and without planetary rotation. The system is initially at radiative-convective equilibrium in a cloud-free condition. Without clouds it will remain motionless (notice that effect of convection is parameterized as instantaneous adjustment to a convectively neutral state and thereby has no effect on driving large-scale dynamics in our models). We initialize a patch of clouds from 0.5 to 0.2 bar centered at the middle of the domain with an exponential decay in the form of $q_{\text{deep}} e^{-(x'/1000 \text{ km})^2}$ where x' is the distance from the domain center. Vapor concentration is initially set to q_{deep} and is homogeneous at pressures greater than 0.5 bar but is zero at pressures less than 0.5 bar. The patch of cloud exerts substantial radiative heating at the cloud base and cooling at the cloud top, which subsequently initiate the circulation. Figure 1 exhibits the time and spatial evolution of cloud mixing ratio on column A, radiative heating and cooling rates on column B, temperature perturbations relative to the initial temperature profile on column C, and stream function on column D. The stream function of the two-dimensional model ψ is defined by $u = -g/L\partial\psi/\partial p$ and $\omega = g/L\partial\psi/\partial x$, where L is the horizontal domain length and u is the horizontal wind. The time sequence starts from time zero in the top row to 37.5 hours of simulated time in the bottom row.

Interestingly, the dynamical evolution quickly differs from that predicted by the linear theory of Gierasch et al. (1973) wherein the cloud patch was expected to initially undergo exponential growth in thickness without wave-like propagation. Instead, radiative heating immediately drives a meridional circulation that splits the cloud patch into two parts that propagate in opposite directions. After the splitting, the cloud layer then starts growing linearly with time while propagating in both flanks. After about 10 hours, a secondary, thinner cloud layer develops at the center of the pattern, which is due to the convergent flow towards the center that uplifts condensable vapor. Eventually when the propagating clouds at different directions encounter each other (notice that the horizontal boundary condition is periodic) after around 20 hours, the model symmetry breaks and

⁴ The Rossby deformation radius is $R_d = c/f$ where c is the phase speed of gravity wave. Using a phase speed of long vertical wave $c \sim 2NH \sim 2000 \text{ m s}^{-1}$ where N is the Brunt-Vaisala frequency and H is scale height, yielding $R_d \sim 10^4$ to 2000 km with $f = 2 \times 10^{-4}$ to $1 \times 10^{-3} \text{ s}^{-1}$. Our horizontal resolution is sufficient to resolve dynamics within the Rossby deformation radius.

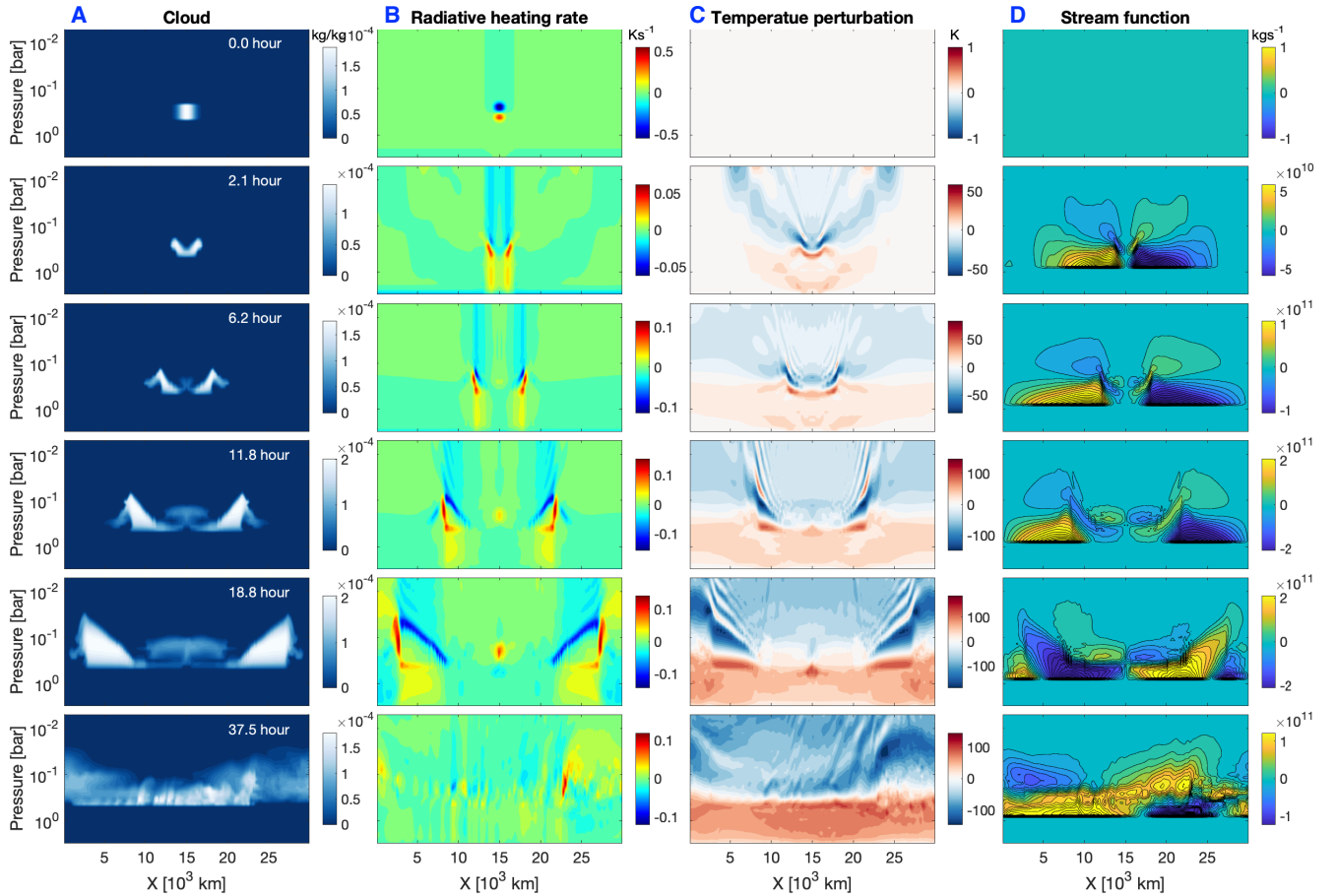


Figure 1. Time evolution of cloud distributions (column A), radiative heating and cooling rates (column B), temperature perturbations (column C) and stream function (column D) in the non-rotating 2D system. In column D, positive values represent counterclockwise and negative values are clockwise. Each row represents the atmospheric state at different model time indicated in the left panels. These are results of the initial evolution of a non-rotating 2D simulation. The model is initially at rest, with a uniform initial cloud-free radiative-convective equilibrium. A patch of cloud is initially placed from 0.5 to 0.2 bar centered at the middle of the domain with an exponential decay in the form of $q_{\text{deep}} e^{-(x'/1000 \text{ km})^2}$ where x' is the distance from the domain center (as depicted in the upper left panel). The vapor concentration is initially q_{deep} and homogeneous below 0.5 bar but is zero above 0.5 bar. The initial cloud patch generates radiative heating and cooling and drives subsequent evolution of the system.

the evolution becomes chaotic.⁵ The predicted linear growth rate $\Gamma_c/(\bar{\Gamma}\tau)$ based on our modeled atmospheric conditions and a reasonable lapse rate for clouds is on the order of 10^{-4} to 10^{-3} s^{-1} , greater than the growth rate of cloud thickness while they propagate horizontally (from 2.1 to 18.8 hours in Figure 1). Although the linear theory predicts a continuous spectrum of unstable modes with similar growth rates, the growing patterns in our simulation are sparse and tend to be large-scale.

The horizontal propagation of the cloud pattern is significantly slower than adiabatic free gravity waves. A crude estimation of phase speed of the adiabatic wave is NH where N is the Brunt-Vaisala frequency and H is scale height, yielding $\sim 1000 \text{ m s}^{-1}$ applying our model condition. This is much faster than the propagation of the cloud pattern, which is only roughly 250 m s^{-1} . A close inspection in the second row of Figure 1, especially in the panels of heating rates, temperature perturbations and stream functions, shows that a

fast component already propagated more than $10 \times 10^3 \text{ km}$ horizontally away from the center in both directions at 2.1 hours. This fast component is roughly consistent with the adiabatic free waves that are triggered by the cloud radiative heating. Strikingly, in later times, vertical wave-like patterns that alternate with decreasing pressure are present above the cloud layers (see panels of heating rate and temperature perturbations at 6.2, 11.8 and 18.8 hours). These patterns do not propagate away like the fast component at 2.1 hours, but rather have a similar horizontal phase speed as the slowly moving cloud patterns and relatively stationary vertical phases—analogue to the forced, quasi-stationary waves.

The differences between our numerical results and the linear theory of Gierasch et al. (1973) in the non-rotating 2D model perhaps partly stem from the intrinsic nonlinearity of the diabatic system—the strong cloud radiative heating depends on all modes that advect the tracer, and is non-separable in some sense. This indicates that different linear modes can be “blended” together by the diabatic heating. This perhaps is why the growing and propagating cloud patterns in Figure 1 are analogous to the triggering of free gravity waves that propagate along opposite directions—the damped but propagating

⁵ A movie of this initial evolution is available at <https://youtu.be/QZHTb20B51Y>.

modes and the growing but non-propagating modes may be blended together, giving rise to the cloud patterns that simultaneously propagate in the horizontal directions and grow in the vertical direction. In addition, the nonlinearity also comes in when eddies grow sufficiently large. As seen in the middle panels in Figure 1, the strongest heating/cooling usually occurs at the edges of cloud patterns. Strong and complex local overturning circulations associated with the heating seem important in affecting the phase speed and growth rate of the pattern. Understanding these detailed complexities is beyond of the scope of this study.

3.1.2 At statistical equilibrium

The circulation does not decay away but eventually evolves towards a chaotic and self-sustained state. After about 40 simulation days, the model reaches a statistical equilibrium state in which gravitational settling of cloud particles is statistically balanced by net upward transport of clouds and condensable vapor. Note that there is still time variability around the time-mean climate state after the model reaches the statistical equilibrium.

Available potential energy (APE) is generated from the spatially inhomogeneous radiative heating/cooling associated with partial cloud coverage, which is converted to kinetic energy (KE) associated with the vigorous circulation. The circulation in turn maintains patchy clouds that are responsible for generation of APE. Kinetic energy is removed mostly by the deep frictional drag, returning to the system via dissipated heat in the deep layers. The fixed bottom boundary temperature (in reality the hot interior of BDs or EGPs) ensures continuous energy supply that offsets radiation to space. The fact that clouds must eventually settle out at low pressures is essential to maintain the circulation—otherwise without settling, clouds will be eventually homogenized above the condensation level and therefore no patchiness would be available to generate APE. The concept of heat engines may be appropriate for the energetics of this system—it has been applied to similar top-cooling-bottom-fueling Earth moist convection (Rennó & Ingersoll 1996) and tropical cyclone systems (Emanuel 1986).

The typical isobaric temperature perturbations in our model can exceed 100 K, and local horizontal wind speeds can exceed 1000 m s^{-1} . Clouds can be easily transported over 3 scale heights above the condensation level. Winds, temperature perturbations and clouds exhibit a wide range of spatial patterns, with horizontal lengthscales ranging about 1000 km to that comparable to the domain length, $3 \times 10^4 \text{ km}$. Structures with lengthscales over $2 \times 10^4 \text{ km}$ are dominant in the vertical transport of clouds and kinetic energy, which evolve over a characteristic timescale of more than 10 hours. The seemingly dominant structure is easier seen in 2D simulations with extended horizontal domains up to $48 \times 10^4 \text{ km}$ shown in Appendix A. The dominant lengthscale for cloud patches is between 2×10^4 to $4 \times 10^4 \text{ km}$, superposed with numerous smaller-scale structure.

One could make use of a quasi-balance point of view to qualitatively understand why the dominant structure emerges at a horizontal lengthscale of 2×10^4 to $4 \times 10^4 \text{ km}$. In statistical equilibrium, large-scale subsidence through a hydrostatic, stratified atmosphere must be accompanied by diabatic cooling (an obvious example would be the Hadley circulation in Earth's troposphere, e.g., Pierrehumbert 2010). In a presumed quasi-stationary overturning circulation, air in the cloudy regions is heated and rises, and it must subsequently cool somewhere and descend due to the requirement of continuity. The rate of radiative cooling determines the velocity of subsiding air,

which can then be used to constrain the typical horizontal lengthscale of the overturning circulation via continuity.

Now we carry out a simple diagnostic scaling exercise based on the governing dynamical equations (Eq.[1] to [4]) to quantify the above picture. More detailed explanation of the scaling based on a similar set of dynamical equations can be found in, e.g., Komacek & Showman (2016) for application on hot Jupiter circulation. It is convenient to cast the primitive equations in log-pressure coordinates (e.g., Andrews et al. 1987; Holton & Hakim 2012). We assume statistical balance (thus the time-dependent terms disappear), and a symmetry between the ascending and the descending branch of the circulation, that they have similar speed, magnitude of heating/cooling rate and thus the fractional area. First, the continuity equation can be expressed as an order-of-magnitude estimation:

$$\frac{\mathcal{U}}{\mathcal{L}} \sim \frac{\mathcal{W}}{H}, \quad (11)$$

where \mathcal{U} is the characteristic horizontal velocity, \mathcal{L} is a characteristic lengthscale of the circulation, \mathcal{W} is a characteristic vertical velocity with a unit m s^{-1} , and H is scale height. In the angular momentum equation, because of the absence of rotation, the major balance is expected between the pressure gradient and advective forces, which in order-of-magnitude is $\mathcal{U}^2/\mathcal{L} \sim \Delta\Phi/\mathcal{L}$ (e.g., Tan & Showman 2017). Hydrostatic balance relates the isobaric temperature gradient to the isobaric geopotential gradient. The vertical difference of geopotential $\delta\Phi$ in a single column is $\delta\Phi = -RT\delta \ln p$, where T is an appropriate vertically-averaged temperature and $\delta \ln p$ is a characteristic thickness of the atmospheric column that is affected by the cloud radiative feedback in log pressure. Thus, the characteristic isobaric geopotential difference between two columns that have a characteristic isobaric temperature difference ΔT is $\Delta\Phi \sim R\Delta T\delta \ln p$. Combining with the angular momentum equation, we have

$$\mathcal{U} \sim \sqrt{R\Delta T\delta \ln p}. \quad (12)$$

The balance in the thermodynamic equation is expected to be between radiative heating/cooling and advection, and is the same for both the ascending and descending branch: $\frac{\delta F}{c_p \delta M} \sim \max\left[\frac{U\Delta T}{\mathcal{L}}, \frac{\mathcal{W}N^2 H}{R}\right]$, where δF is the radiative flux difference in-and-out of the atmospheric column with mass δM . The two terms on the right hand side are horizontal and vertical heat transport, respectively. Based on our simulated results, the term $N^2 H^2/R$ is usually larger than ΔT , so together with the continuity Equation (11) we expect that the balance in the thermodynamics is between vertical advection and radiative heating/cooling:

$$\frac{\delta F}{c_p \delta M} \sim \frac{\mathcal{W}N^2 H}{R}. \quad (13)$$

Using all the balances in equations (11), (12) and (13), we are in the position to estimate the typical lengthscale of the overturning circulation

$$\mathcal{L} \sim \frac{c_p \delta M (NH)^2}{\delta F} \sqrt{\frac{\Delta T \delta \ln p}{R}}. \quad (14)$$

We apply the following numbers based on diagnostic result of our simulations: $(NH)^2 \sim 10^6 \text{ m}^2 \text{ s}^{-2}$, $\delta F \sim 10^5 \text{ Wm}^{-2}$, $\delta M = \delta p/g \sim 5 \times 10^5/10^3 \text{ kg}$ (the thermal response of an atmospheric column to clouds extends far deeper than the assumed condensate level of 0.5 bar, and here we set $\delta p \sim 5$ bars based on our numerical results), $\Delta T \sim 100 \text{ K}$ and $\delta \ln p \sim 4$. The resulting characteristic lengthscale is about $\mathcal{L} \sim 1.9 \times 10^4 \text{ km}$, consistent with numerical results.

In a short summary, in the absence of planetary rotation and under our assumed atmospheric conditions, a typical horizontal lengthscale

on the order of $\sim 2 \times 10^4$ km is required for the hot air to cool and return to the altitude where it was heated up, which is a requirement for a closed thermodynamic loop of the air. Failing to provide a sufficiently large simulated domain in a non-rotating 2D system may result in suppression of the self-maintained dynamics. This is because there is not sufficient room for the air to cool and descend, and thus no flow can be lifted up to form new clouds due to continuity and the initial clouds would gradually settle down. As a result, the response of the simulated atmosphere to the initial perturbation is simply to cool down as a whole towards the cloud-free equilibrium. Indeed, we tested a model with domain size 1.5×10^4 km (half of the default value), and the model eventually became quiescent no matter how strong an initial perturbation was applied.

3.2 Three-dimensional dynamics and the importance of rotation

3.2.1 Initial evolution

Planetary rotation plays a fundamental role in shaping the large-scale dynamics of rapidly rotating BDs and directly imaged EGPs (Showman & Kaspi 2013). One of the profound consequences of rapid rotation on the stratified, thin atmosphere is the emergence of a major balance between the rotation and horizontal pressure gradient, which strongly affects the scale of flows, transport of tracers and typical horizontal temperature variations. Rotation leads to a natural dynamical lengthscale — the Rossby deformation radius $R_d = c/f$ where c is the phase speed of gravity wave, a lengthscale over which many types of interesting dynamical phenomena occurs (e.g., Vallis 2006).

In the inertia gravity wave system of Gierasch et al. (1973), when f is large, unstable modes associated with cloud radiative instability are only possible for small horizontal lengthscales. For the quasi-balanced flow under rapid rotation (the so-called quasi-geostrophic flow), unstable modes are possible for axisymmetric modes, i.e., flows associated with coherent vortices. Growth rates of the axisymmetric modes are greater for larger horizontal wavenumber (smaller horizontal lengthscale). The instability ceases when the lengthscale becomes much greater than the deformation radius, because over large lengthscales the vertical motions tend to be inhibited by rotation.

Similar to the exercise in Section 3.1.1, we investigate the initial-value problem to see how rotation shapes the dynamical evolution, but now in a 3D model with a double-periodic horizontal boundary condition and a constant Coriolis parameter $f = 6 \times 10^{-4} \text{ s}^{-1}$. Similarly, the 3D model is initialized with a patch of clouds from 0.5 to 0.2 bar centered at the middle of the domain with an exponential decay in the form of $q_{\text{deep}} e^{-(r/1000 \text{ km})^2}$ where r is the horizontal distance to the domain center. Vapor concentration is initially q_{deep} and homogeneous at pressures larger than 0.5 bar but is zero at pressures less than 0.5 bar. The spatial and time evolution of cloud mixing ratio at 0.23 bar is shown in Figure 2, in which each panel shows the instantaneous cloud mixing ratio in color contours and the wind field in arrows. The time of each frame is indicated above each panel.

The initial evolution is essentially a geostrophic adjustment, a process by which an initially unbalanced perturbation is adjusted towards the geostrophic balance — a balance between the pressure gradient force and the Coriolis force (e.g., Holton & Hakim 2012; Gill & Donn 2016). Radiative heating associated with the initial cloud patch generates a strong positive temperature anomaly over a short time after initialization, which drives a subsequent outflow from the cloudy

region. The outward winds are then deflected towards their right by rotation, and a strong anticyclone forms around the cloud pattern.⁶ In this configuration, the Coriolis force tends to balance the outward pressure gradient force. Residual outward flow still persists despite the major geostrophic balance that is quickly established. This residual flow is responsible for the continuous horizontal growth of the cloud pattern until the size of the vortex saturates at about 4.5×10^3 km in radius. In the classic geostrophic adjustment problem wherein an initially unbalanced field is freely evolved without forcing and dissipation, the final equilibrium height (or pressure) field is predicted to be characterized by an exponential decay with a characteristic lengthscale of a deformation radius (e.g., Kuo & Polvani 1997; Gill & Donn 2016). The deformation radius in conditions relevant to our simulations may be estimated using a phase speed of long vertical wave $c \sim 2NH$, yielding $R_d \sim 3.3 \times 10^3$ km, which is roughly consistent with the prediction by the much simpler classical geostrophic adjustment theory despite the more complex dynamical process in our system.

The circulation and cloud pattern before about 40 hours are dominated by a basic state that is axisymmetric around the center of the initial cloud patch. This is consistent with predictions by the quasi-geostrophic cloud radiative instability (Gierasch et al. 1973). The basic state is superimposed by a seemingly wavenumber-4 non-axisymmetric component starting from 16.7 hour, and this particular component does not amplify as the evolution goes on. Eventually after about 50 hours, the basic axisymmetric circulation breaks, and multiple vortices emerge from a wavenumber-3 non-axisymmetric component at the end of the sequence shown in Figure 2. The initial non-axisymmetric component may be a result of instability of the anticyclone. One possibility is that a vortex initially embedded in an environment at rest may be unstable due to instability analogous to the shear instability (e.g., see a recent work by Reinaud & Dritschel 2019 for quasi-geostrophic vortices). The other possibility is the inertial instability, which may occur when the absolute angular momentum $\mathcal{M} = rV + \frac{1}{2}fr^2$ of the vortex decreases with increasing radial distance ($f \frac{\partial \mathcal{M}}{\partial r} < 0$, e.g., Holton & Hakim 2012), where r is the radial distance and V is the azimuthal velocity of the vortex. We have confirmed that the criteria $f \frac{\partial \mathcal{M}}{\partial r} < 0$ is indeed satisfied at the pressure level shown in Figure 2 very soon after the initialization. The unstable region is mostly near the outer edge of the anticyclone where the speed of the clockwise azimuthal wind rapidly increases with r .

Compared to the non-rotating results in Figure 1, we find that rotation significantly confines the horizontal extent of the circulation and cloud pattern. For example, at about 16.7 hours after the initialization, the edge of the cloud pattern only extends out to roughly 3000 km away from the center in the case with $f = 6 \times 10^{-4} \text{ s}^{-1}$, whereas that in the non-rotating 2D system already reaches more than 12000 km away from the center. Our finding is qualitatively consistent with the conceptual understanding of the quasi-geostrophic, cloud radiative instability theory of Gierasch et al. (1973), showing that the typical horizontal lengthscale of the cloud-radiative-driven circulation can be limited to a scale close to the deformation radius.

3.2.2 Dynamics at statistical equilibrium with varying f

Similar to the 2D system, the 3D system shown in Figure 2 eventually evolves to a highly nonlinear and chaotic state in statistical

⁶ A cyclone has relative vorticity the same sign as the local planetary rotation, whereas the anticyclone has the opposite sign of relative vorticity.

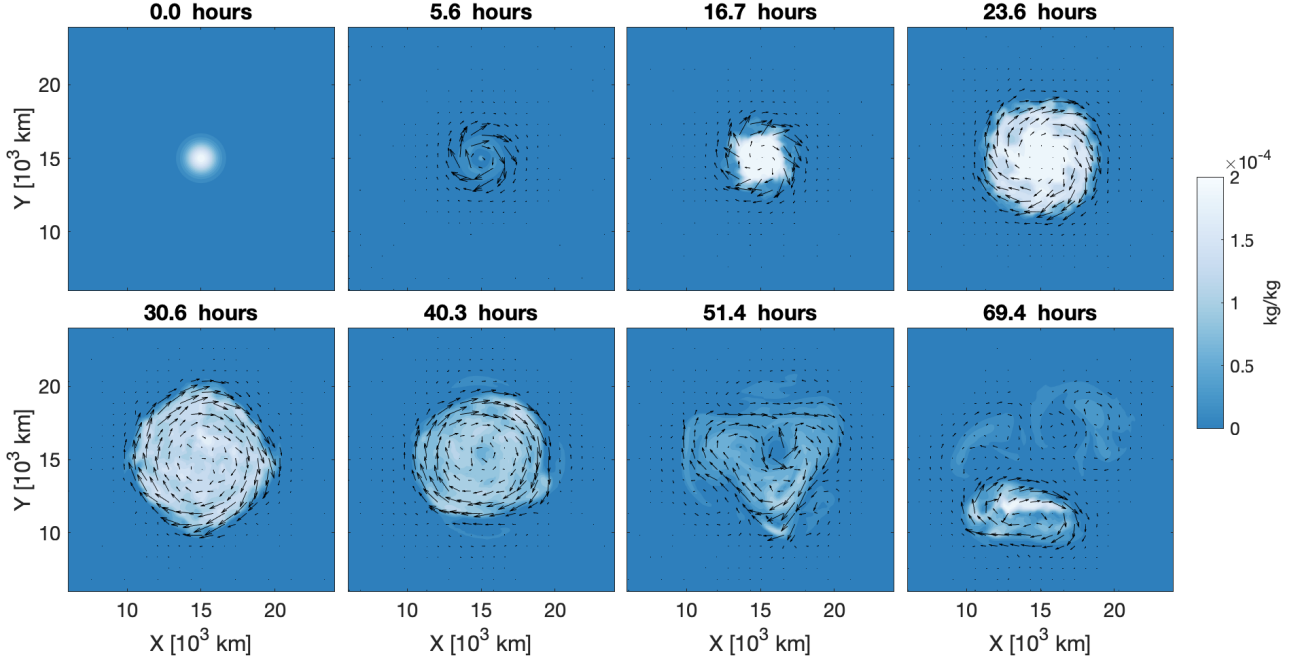


Figure 2. Time evolution of cloud distribution in a 3D simulation with a constant Coriolis parameter $f = 6 \times 10^{-4} \text{ s}^{-1}$. Color contours in each panel represent the instantaneous cloud mixing ratio at different time and at pressure 0.23 bar, and arrows represent the horizontal wind vectors. The model is initially at rest, with an uniform initial cloud-free radiative-convective equilibrium, and no clouds except in a small area centered around $X, Y = 15$ depicted in the upper left panel. Note that these panels are zoomed in.

equilibrium that is self-sustained by cloud-radiative feedback. To systematically investigate the effect of rotation on the equilibrated states, we first performed a set of 3D simulations with varying Coriolis parameters from $f = 0$ to $1 \times 10^{-3} \text{ s}^{-1}$ over a fixed domain size ($30000 \text{ km} \times 30000 \text{ km}$). Selected results of the equilibrated simulations with $f = 0, 3 \times 10^{-4}, 6 \times 10^{-4}$ and $1 \times 10^{-3} \text{ s}^{-1}$ (corresponding to f at polar regions of objects without rotation and with rotation periods of 11.6, 5.8 and 3.5 hours, respectively) are shown in Figure 3, in which the left column shows instantaneous cloud mixing ratio as 0.23 bar with horizontal wind vectors represented by arrows, the middle column shows the corresponding instantaneous temperature field with wind vectors at 0.23 bar, and finally the corresponding top-of-atmosphere thermal flux is shown the right column. Panels at different rows have different Coriolis parameters f as indicated above each panel.

The typical sizes of storms and vortices decrease with increasing rotation, as can be seen in Figure 3. When there is no background rotation ($f = 0$), dynamics in the 3D simulation are characterized by domain-scale convergent and divergent flows which are qualitatively similar to those in the non-rotating 2D simulation. When rotation is included, the simulated domain at 0.23 bar is populated with anticyclones that are warmer and cloudy, and cyclones that are associated with relatively cloudless and cooler regions. Significant isobaric temperature variations over 100 K are present in all models. There exists significant variation of the isobaric cloud mixing ratio, ranging from almost zero to more than the deep mixing ratio q_{deep} . Cloudy regions are usually accompanied with vigorous upwelling and cloud-free regions are associated with strong downwelling. The outgoing thermal flux exhibits strong variation across the domain, with more than $6 \times 10^5 \text{ Wm}^{-2}$ at cloudless regions and only slightly more than $3 \times 10^5 \text{ Wm}^{-2}$ at cloudy regions. This is consistent with our expectation that cloud opacity determines the level from which

thermal flux escapes to space. Interestingly, anticyclones with cloud formation almost always have larger sizes than the cloudless cyclones.

Vertical thermal profiles are shaped by both the cloud-radiative effect and the dynamics. Figure 4 shows several instantaneous temperature-pressure (T-P) profiles sampled in the cloudy (red lines) and cloudless (black lines) regions of the model with $f = 6 \times 10^{-4} \text{ s}^{-1}$ in the top panel and those sampled in the model with $f = 0$ in the bottom panel. In the rapidly rotating case, the cloudy regions exhibit a characteristic cold top and hot bottom structure, whereas the cloudless regions are more isothermal above 1 bar which is closer to the thermal structure that would occur in cloud-free radiative-convective equilibrium. In the cloudy regions, clouds form above the condensation level (which is assumed at 0.5 bar), and their greenhouse effect warms up the air below the condensation level. The greenhouse effect extends down to about 5 bars, below which the temperature profiles merge to the same deep adiabatic profile that is specified by our bottom boundary condition. Above the condensation level, the atmospheric lapse rate $d \ln T / d \ln p$ is larger in the cloudy region because of the top cooling and bottom heating due to cloud opacity. Clouds usually extend more than one scale height above the condensation level, which, together with the large lapse rate, result in a characteristic crossing point between two sets of T-P profiles above the convective zone. Thermal flux escapes from cloudless regions at pressures of several bars where is hot, and thermal flux of cloudy regions is emitted from the much colder cloud-top.

Dynamics is important to determine the thermal structure seen in Figure 4 both explicitly and implicitly. Explicitly, temperature fluctuations with smaller vertical wavelength are caused by the inertia gravity waves. They are present in both cloudy and cloudless regions. Implicitly, although cloud opacity is the direct cause of the typical thermal structures, both the cloud and temperature anomaly need to resist fast-travelling gravity waves that efficiently remove

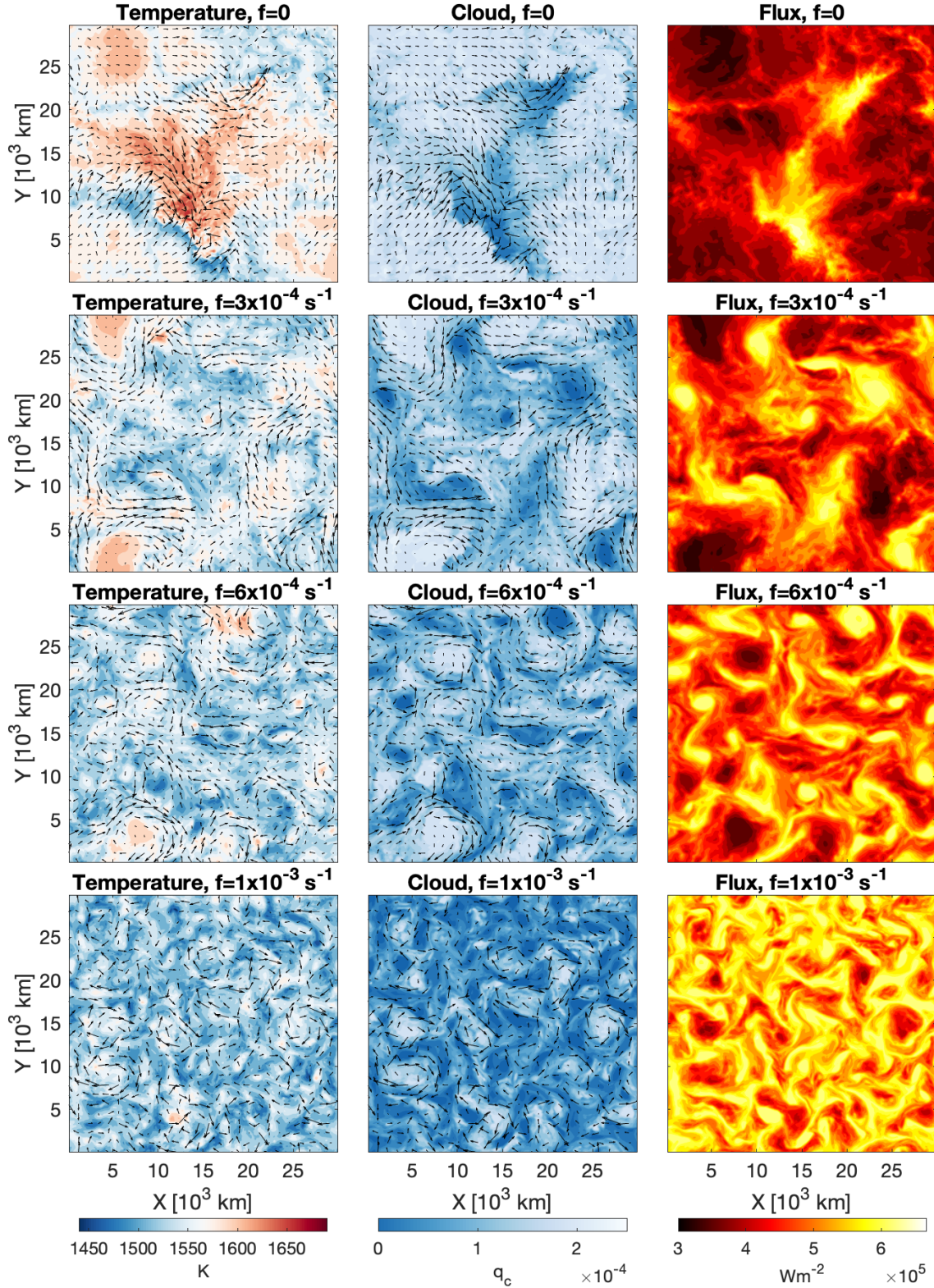


Figure 3. Instantaneous horizontal cloud mixing ratio at 0.23 bar on the left column, and the corresponding temperature at 0.23 bar on the middle, and the corresponding outgoing top-of-atmosphere thermal flux on the right. Arrows represent instantaneous horizontal wind vectors. These are results from models with different Coriolis parameters $f = 0$ (top row), 3×10^{-4} (second row), 6×10^{-4} (third row) and $1 \times 10^{-3} \text{ s}^{-1}$ (bottom row). The model domain size is fixed at $30000 \text{ km} \times 30000 \text{ km}$. Other parameters are the same among these models.

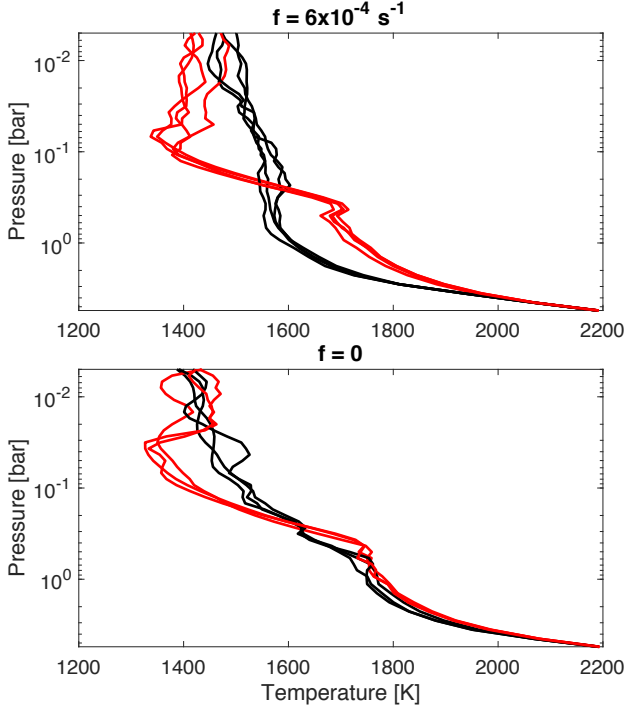


Figure 4. Selected instantaneous temperature-pressure profiles for cloudy regions (red lines) and cloudless regions (black lines) for simulations with a Coriolis parameter $f = 6 \times 10^{-4} \text{ s}^{-1}$ in the top panel and $f = 0$ in the bottom panel.

anomalies. Rotation plays an essential role in two key ways. First, the quasi-geostrophic balance due to rotation helps to sustain a large isobaric temperature difference (Charney 1963). Second, local overturning circulations associated with vortices formed under rotation are likely important for vertical transport of clouds, and they typically evolve much slower than gravity waves. Therefore, the vertical cloud structure can be sustained long enough for the radiative effects to be effective. Indeed, T-P profiles in the non-rotating simulations (the bottom panel of Figure 4) have much smaller temperature differences between the cloudy and relatively cloudless regions.

The time evolution of the dynamical system is intriguing. Vortices are vulnerable and undergo straining, merging and dissipation over time. An individual anticyclone or cyclone usually evolves over a timescale of several to tens of hours. Inertia gravity waves are characterized by smaller length scales than the dominant vortices, evolving with a faster frequency and phase speed than the major vortices. The thickest cloud decks are usually formed in the mature anticyclones where vigorous upwelling helps to sustain clouds against gravitational settling. A growing anticyclone usually originates from a small perturbation that triggers a small patch of clouds. Then the geostrophic adjustment process discussed in Section 3.2.1 is driven by the cloud radiative feedback and initialize the growth of vortices. However, not all “seed” clouds are able to grow. Most of the time, small cloud patches are sheared apart or strained away by the turbulent flow, and only the lucky ones survive and are able to grow.

The size of the dominant vortices approximately linearly decreases with increasing f (Figure 3), and now we further quantify the horizontal size distribution of various quantities. Individual vortices are chaotic and unpredictable, and their statistical properties can be uncovered using power spectral analysis in wavenumber space.

Assuming that the flow is statistically isotropic in the horizontal direction, we can express the power spectra in the total wavenumber space $|\mathbf{k}| = \sqrt{|\mathbf{k}_x|^2 + |\mathbf{k}_y|^2}$ where \mathbf{k}_x and \mathbf{k}_y are wavenumber vector in x and y direction, respectively. Figure 5 shows time-averaged power spectra for $KE = (u^2 + v^2)/2$ in the upper left, variance of temperature perturbations T'^2 in the upper right, and variance of total tracer mixing ratio perturbations q'^2 at the lower left, all of which are analyzed at pressure 0.23 bar. On the lower right we show the power spectra for the variance of outgoing thermal flux perturbations F'^2 . These are from models with Coriolis parameters $f = 1 \times 10^{-4}, 2 \times 10^{-4}, 3 \times 10^{-4}, 4 \times 10^{-4}, 6 \times 10^{-4}, 8 \times 10^{-4}$ and $1 \times 10^{-3} \text{ s}^{-1}$. The horizontal axis is in unit of $2\pi/\text{wavelength}$. Note that these simulations are carried out with the same simulated domain size as shown in Figure 3. The energy containing wavenumber, which is defined as $k_e = \left[\frac{\sum_{k \geq 1} k^{-1} E(k)}{\sum_{k \geq 1} E(k)} \right]^{-1}$, where $E(k)$ is the power at wavenumber k (e.g., Schneider & Liu 2009), are plotted as vertical dashed lines for each power spectra for KE , q'^2 and flux variance.

The most prominent feature of the power spectra for KE and q'^2 at 0.23 bar and F'^2 is that the peaks of the spectra systematically shift from the smallest wavenumber (the largest wavelength) to larger wavenumbers (smaller wavelength) as f increases. The energy containing wavenumber k_e also systematically increases with increasing f , although the k_e sometimes differ slightly from the wavenumber where the spectra peaks. With a fixed f , peaks of power spectra for the above three quantities are almost the same. For simulations with $f = 1 \times 10^{-4}$ and $f = 2 \times 10^{-4} \text{ s}^{-1}$, their dominant horizontal structure is comparable to the domain size and therefore their power spectra peak at the smallest wavenumber. The power spectra of T'^2 at 0.23 bar differ from those for the other three quantities, especially for those with $f \geq 3 \times 10^{-4}$. Not only the spectral peaks of T'^2 generally differ with those of the other three quantities given a fixed f , but also the T'^2 power spectra show double local peaks when f is relatively large. The similar spectral shape between F'^2 and q'^2 but not between F'^2 and T'^2 quantitatively demonstrates that patchy clouds (and therefore the cloud-top temperature variations) are the dominant factors shaping the outgoing thermal flux variability, and that isobaric temperature variation is a side effect. Indeed, analysis of observed near-IR spectral time variability for several BDs (e.g., Buenzli et al. 2012; Apai et al. 2013; Lew et al. 2016, 2020), in which detailed static 1D atmospheric models were fit to the spectral variability, have shown that changes of cloud vertical structures are essential, and that temperature anomalies as well as the corresponding gas chemical variation help to improve the fit.

The KE spectra also help to infer the typical behaviors of the turbulence. Pure 2D turbulence tends to transfer kinetic energy from small to large scale starting from where energy is injected—the so-called upscale KE transfer of 2D turbulence. This results in a characteristic KE power spectral slope of $-5/3$: $E(k) \propto k^{-5/3}$ in the so-called inertial range with lengthscales larger than the energy injection scale. In the meantime, transport of enstrophy (the square of potential vorticity integrated over the domain) from large to small scales leads to a KE power spectral slope of -3 : $E(k) \propto k^{-3}$ in the inertial range where the lengthscale is smaller than the injection scale. Large-scale turbulence in the rapidly rotating, stratified atmospheres has similar properties to the 2D turbulence (Charney 1971). For a comprehensive tutorial of incompressible and geostrophic turbulence related to atmospheric applications, see Chapter 8 and 9 of Vallis (2006). In the KE power spectra at 0.23 bar shown in Figure 5, for $f \geq 3 \times 10^{-4} \text{ s}^{-1}$, the spectral peaks roughly locate at the scale of the internal deformation radius $L_d = c_g/f$, where c_g is the phase

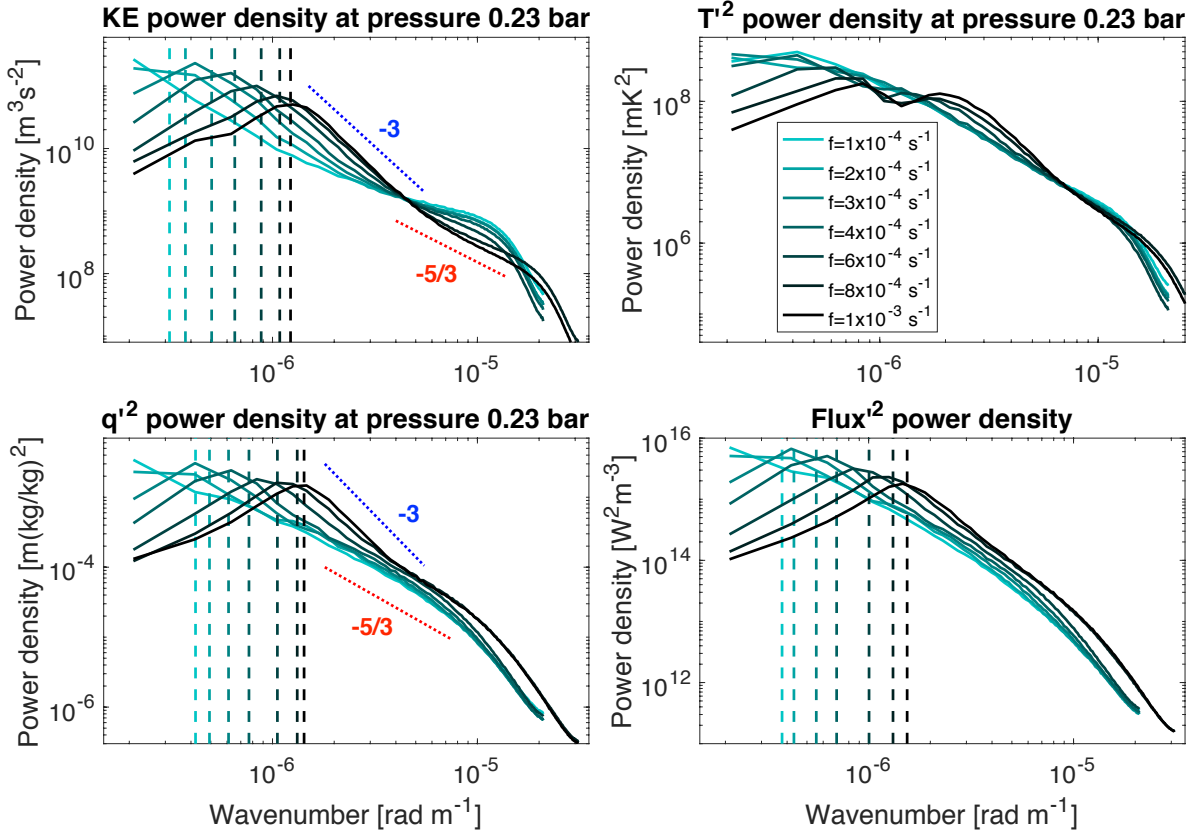


Figure 5. Time-averaged power spectra of kinetic energy (KE, top left), variance of isobaric temperature perturbations T'^2 (top right), variance of isobaric total tracer perturbations q'^2 (bottom left) and variance of the outgoing top-of-atmosphere thermal flux F'^2 (bottom right) as a function of the total wavenumber k . The former three quantities are taken at pressure 0.23 bar. Different line colors are for cases with different Coriolis parameters from $f = 1 \times 10^{-4} \text{ s}^{-1}$ to $f = 1 \times 10^{-3} \text{ s}^{-1}$. Spectral slopes of -3 and $-5/3$ are indicated as dotted lines in the panels for KE and q'^2 . Vertical dashed lines represent the energy containing wavenumber k_e of each power spectra (see definition of k_e in the text). k_e is not plotted for T'^2 spectra because the presence of double peaks in some spectra makes k_e less representative.

speed of gravity waves. The KE power then decreases with increasing wavenumber in a characteristic slope close to -3 (a blue dotted line indicating a -3 slope is shown in the top left of Figure 5). However, at some point the KE spectra flattens out, and then its slope increases again at very large wavenumber. For relatively small f , the spectral range with a -3 slope is smaller than that of larger f , and the transition to flatter spectra occurs at a wavenumber that is closer to the peak for cases with smaller f . For $f \lesssim 4 \times 10^{-4} \text{ s}^{-1}$, the KE spectral slope can be flatter than a $-5/3$ power law (a red dotted line indicating a $-5/3$ slope is plotted) whereas those with $f \gtrsim 6 \times 10^{-4} \text{ s}^{-1}$ is closer to $-5/3$. Interestingly, the q'^2 spectra similarly exhibit a slope transition between -3 to $-5/3$ only when f is quite large.

The spectral features suggest a few interesting dynamical processes at 0.23 bar. First, KE at 0.23 bar is likely injected directly around the lengthscale close to the internal deformation radius via geostrophic adjustment. Then, enstrophy of the turbulence cascades from the deformation radius to smaller scales, showing a characteristic KE spectral slope of -3 . Turbulence in the slope $= -3$ range has a quasi-geostrophic nature. Second, in the spectral space where the slope is flatter than -3 , non-2D turbulence (possibly inertia gravity waves) becomes energetically important in the KE power spectra. It has been known that the Earth’s upper troposphere exhibits a transition between a -3 KE spectral slope at large scale to a $-5/3$ slope at mesoscale (Nastrom et al. 1984). Non-2D turbulence likely contributes to this transition (e.g., Dewan 1979; Lindborg 1999, 2007).

In our simulations, inertia gravity waves may play this role. Indeed, flows with scales close to the deformation radius are close to geostrophic balance, indicating a quasi-2D nature. Flows with much smaller scales have large components of imbalanced inertia gravity waves. This was confirmed by investigating the relative fractions of the rotational and divergent parts of the horizontal velocity at different lengthscales. For models with smaller f , the degree of geostrophic balance is weaker, and inertia gravity waves are likely more important in the energetics than in models with larger f . Interestingly, the transition between slope -3 to $-5/3$ depends on the forcing amplitude as well. In Section B in the Appendix, Figure B1, we show that when the model with $f = 4 \times 10^{-4} \text{ s}^{-1}$ is forced progressively weaker, the KE spectra at 0.23 bar exhibits a slope -3 all the way to large wavenumber before numerical dissipation takes over. When the wavenumber continues increasing toward the largest value, numerical dissipation near the grid scale becomes important and the spectral slope deepens. Third, at wavenumbers smaller than that of the deformation radius (larger lengthscales), KE is transferred upscale. However, at large scales, KE is strongly dissipated by the bottom frictional drag, so that the KE power spectra decreases as the wavenumber decreases. We shall discuss this point more in Section 3.4.

Finally we summarize dynamics with varying rotation in Figure 6 with various statistical quantities for simulations as a function of f (see the caption of Figure 6 for a description). There exist interesting

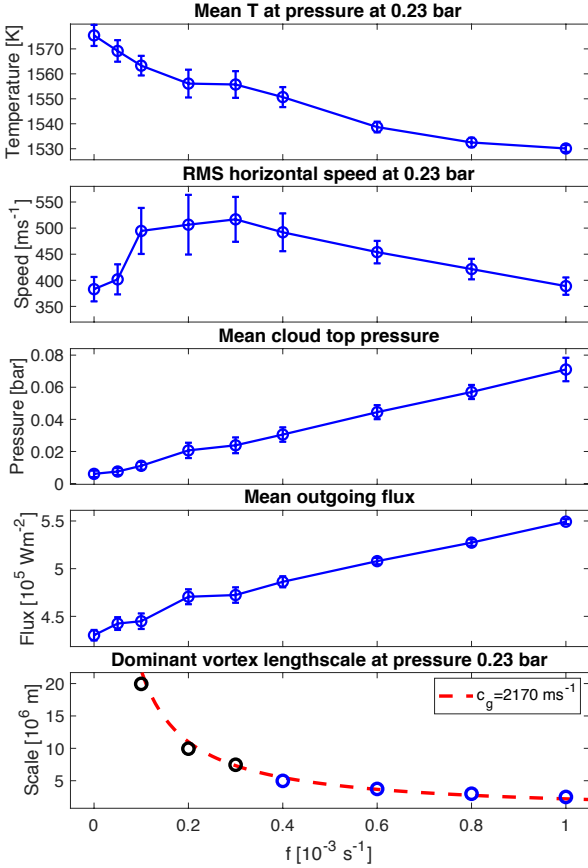


Figure 6. Various statistical quantities that are averaged over the horizontal domain and time from models with varying Coriolis parameters from $f = 0$ to $f = 1 \times 10^{-3} \text{ s}^{-1}$. Errorbars in some panels are the variance of the horizontal mean quantities with respect to time, and therefore they represent the time fluctuation of the instantaneous horizontal-mean field. All data in blue are from models with a fixed model domain size of $30000 \text{ km} \times 30000 \text{ km}$. Panel (a) is for the horizontal temperature at 0.23 bar; panel (b) is for the RMS of horizontal wind speed at 0.23 bar; panel (c) is for the mean cloud-top pressure, which is arbitrarily defined as where the horizontal-mean cloud mixing ratio is equal to $2 \times 10^{-6} \text{ kg kg}^{-1}$; panel (d) is for the outgoing top-of-atmosphere thermal flux; and finally panel (e) is for the dominant vortex size defined as π/k_{max} , where k_{max} is the wavenumber with the maximum KE power. Note that in panel (e), black circles for $f = 1 \times 10^{-4}$, 2×10^{-4} and $3 \times 10^{-4} \text{ s}^{-1}$ are from models with domain size properly extended, which is to properly capture the statistical vortex behaviors. In panel (e), the dashed curve is a fit to the vortex size using the deformation radius $L_d = c_g/f$ with a fitted gravity wave phase speed c_g , yielding $c_g = 2170 \text{ ms}^{-1}$.

trends with f . Mean temperature at 0.23 bar monotonically decreases with increasing f , while the mean outgoing thermal flux and mean cloud top pressure monotonically increase with increasing f . These three trends are linked. As rotation increases, the mean thickness of clouds decreases, resulting in an increase of the cloud-top pressure and thus an increase of outgoing thermal flux due to the higher cloud-top temperature. The cloud greenhouse effect is weakened by the reduction of clouds, and thus the temperature at 0.23 bar decreases with increasing f .

The wind speed at 0.23 bar shows a steep increase from $f = 0$ to $f \sim 1 \times 10^{-4} \text{ s}^{-1}$, and then only slight increases till $f \sim 3 \times 10^{-4} \text{ s}^{-1}$, after which it mildly declines with increasing rotation rate. This trend probably indicates the degree of geostrophic balance established in

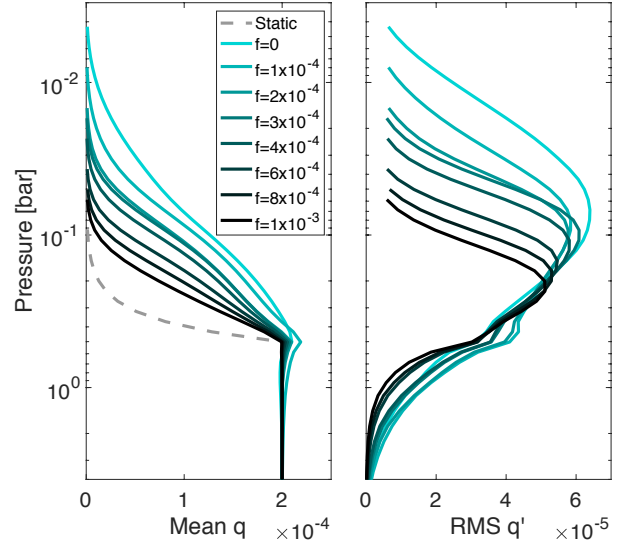


Figure 7. Left panel: the time- and horizontal-mean mixing ratio of total tracer (gas+cloud particles) as a function of pressure for simulations with $f = 0$ to $1 \times 10^{-3} \text{ s}^{-1}$. The dashed line is the tracer profile in the absence of dynamics (i.e., it follows q_s in Equation (8) above 0.5 bar and q_{deep} below 0.5 bar). Right panel: the time-mean RMS of the isobaric tracer mixing ratio perturbation as a function of pressure.

systems with a fixed domain size. At $f = 0$, dynamics are dominated by gravity waves. Although significant isobaric temperature differences must exist due to the cloud radiative effect, gravity waves are still efficient in removing large horizontal temperature gradients across most of the domain (see Figure 4). With a small f , a finite deformation radius emerges and vortices form, helping to sustain larger isobaric temperature variation than the non-rotating case. In this case the deformation radius is larger or comparable to the domain size, such that slight increases of f greatly help sustain a larger temperature gradient. This may help to explain the rapid trend when f is small. When f is sufficiently large and the deformation radius is smaller than the domain size, more vortices are populated in the domain, and the trend of increasing temperature gradient flattens. When f is further increased, the deformation radius becomes a small fraction of the model domain. In this regime, the horizontal wind speed scales as $U \sim (R\Delta T \delta \ln p)/(Lf)$ where L is a characteristic length scale of the vortices. L is loosely proportional to the deformation radius and thus Lf remains a rough constant. Therefore wind speed scales with the characteristic horizontal temperature variation. As has been shown, cloud radiative forcing declines with increasing f , and as a result, the decrease of ΔT then slows the wind speed with increasing f .

As we expected, when the deformation radius is much smaller than the domain size, the horizontal scale of dominant vortices linearly depends on $1/f$ (see panel [e] of Figure 6). The fit using a deformation radius $L_d = c_g/f$ fits well to the vortex lengthscale with a gravity phase speed $c_g = 2170 \text{ ms}^{-1}$. This is consistent with our previous estimate using a long vertical wave phase speed $2NH \sim 2000 \text{ ms}^{-1}$.

3.3 Vertical tracer transport

One of the profound impacts of rotation on the dynamical system is that the thickness of cloud layers decreases with increasing rotation.

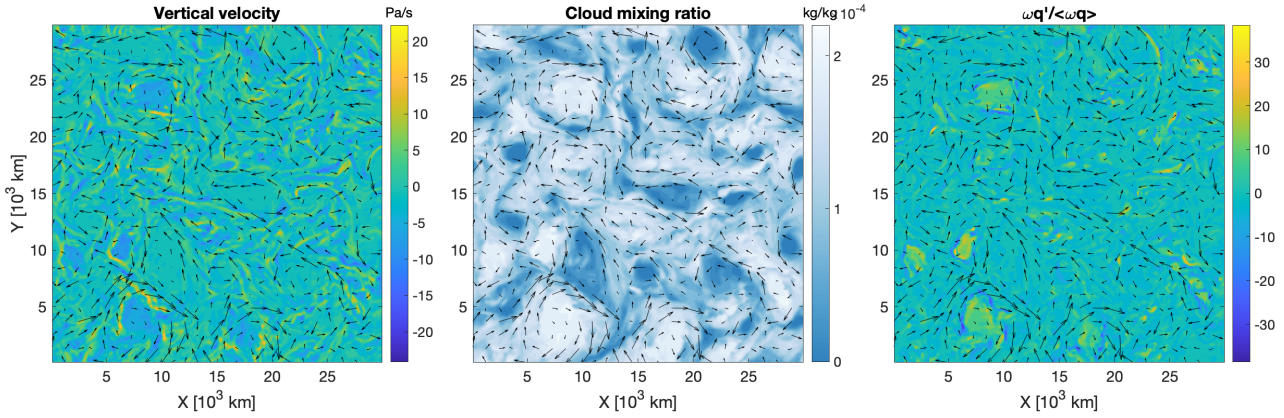


Figure 8. Left panel: instantaneous vertical velocity at pressure coordinates at 0.23 bar for a simulation with $f = 6 \times 10^{-4} \text{ s}^{-1}$. Arrows represent horizontal wind vectors. Middle panel: instantaneous cloud mass mixing ratio at 0.23 bar. Right panel: corresponding $\omega q'_c / \langle \omega q_c \rangle$ at 0.23 bar.

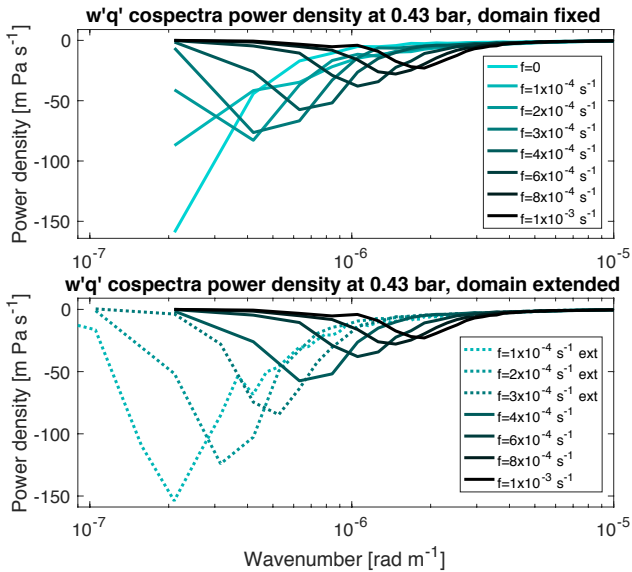


Figure 9. Top panel: cospectral power density for $\omega' q'$ at 0.43 bar (the cloud base) for models with different Coriolis parameters from $f = 0$ to $1 \times 10^{-3} \text{ s}^{-1}$. All models in the top panel have a fixed domain size of $30000 \times 30000 \text{ km}$. Bottom panel: dotted lines for models with $f = 1 \times 10^{-4}, 2 \times 10^{-4}$ and $3 \times 10^{-4} \text{ s}^{-1}$ with properly extended domain size to capture the statistical vortex behaviors. The same models with $f = 4 \times 10^{-4}, 6 \times 10^{-4}, 8 \times 10^{-4}$ and $1 \times 10^{-3} \text{ s}^{-1}$ as the top panel are also plotted as solid lines in the bottom panel.

We emphasize that the cloud condensation level is intentionally fixed at 0.5 bar at all horizontal locations, such that the change of mean cloud thickness is solely due to the change of rotation. The left panel in Figure 7 shows time- and horizontal-mean total tracer (gas and clouds) mixing ratio as a function of pressure for simulations with $f = 0$ to $1 \times 10^{-3} \text{ s}^{-1}$. The right panel contains the time-mean RMS of the isobaric total tracer mixing ratio perturbation q' as a function of pressure. The overall mean tracer mixing ratio smoothly decreases with increasing rotation rate, and is the same with the RMS q' . Intuitively, one might imagine that the stronger the rotation, the greater the suppression of the vertical velocity due to the higher tendency towards geostrophic balance, making the flow less efficient to verti-

cally transport tracers against gravitational settling. This results in smaller horizontal temperature anomalies via the weakened cloud radiative feedback, which then give rise to a positive feedback to the reduced vertical velocity. In this subsection we quantify the net vertical transport of tracers with varying f and at different pressure.

Net upward transport of tracers across an isobaric surface relies on the positive correlation of tracer abundance and vertical velocity, i.e., having upwelling at regions where tracers are more abundant and downwelling at regions with lower tracer abundances (e.g., Holton 1986; Parmentier et al. 2013; Zhang & Showman 2018; Komacek et al. 2019). In a statistically balanced state, the horizontal mean total tracer abundance is set by a balance between the net vertical transport by large-scale motions and gravitational settling of clouds:

$$\frac{\partial \langle \omega' q' \rangle}{\partial p} = - \frac{\partial \langle q_c V_s \rangle}{\partial p}, \quad (15)$$

where $q = q_c + q_v$ is the total tracer and \bar{A} denotes a horizontal average of quantity A over the domain. Integrating Equation (15) from very low pressure where tracers are negligible to an arbitrary level where clouds are abundant, one obtains $\overline{\omega' q'} = -\overline{q_c V_s}$ at that level. This states that the net upward transport of total tracers across that isobar balances the total settling flux above that isobar. Regions with abundant clouds likely have strong radiative heating near the cloud base and cooling near the cloud top, whereas relatively cloudless regions usually radiatively cool. This typically results in upwelling at cloudy regions and downwelling at cloud-free regions, which naturally represents a mechanism for net upward tracer transport against gravitational settling.

The questions are, what type of motions are responsible for the major vertical transport and how do they depend on rotation? As seen from Figure 3 and their time evolution, as well as the power spectral properties of KE and q' shown in Figure 5, the size of cloud patches are comparable to the dominant vortex scales and are highly correlated to the flow pattern. Thus we would expect that the dominant tracer transport near the condensation level is by the overturning flow associated with cloud-forming vortices. Figure 8 shows instantaneous vertical velocity (with a unit of Pa s^{-1}) at 0.23 bar for the model with $f = 6 \times 10^{-4} \text{ s}^{-1}$ on the left panel, the corresponding cloud mixing ratio on the middle panel and the corresponding quantity $\omega q'_c / \langle \omega q_c \rangle$ (the brackets mean horizontal averaging) on the right panel. The latter quantity measures the correlation between tracer abundance and vertical velocity, with positive meaning upward transport and vice versa (Parmentier et al. 2013). A few mature anticyclones show obvious

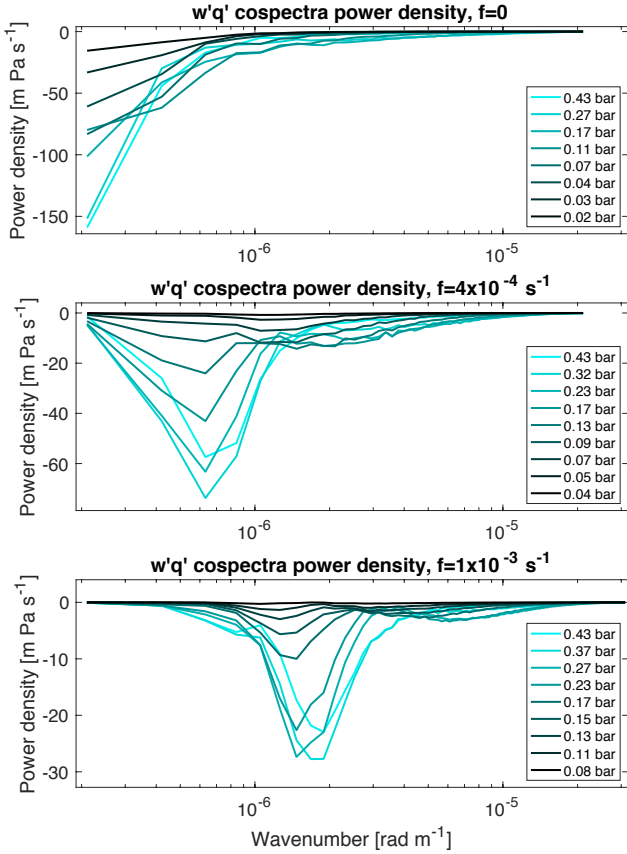


Figure 10. Cospectral power density for $\omega'q'$ at different pressures for simulations with different Coriolis parameters $f = 0$ (top panel), $f = 4 \times 10^{-4} \text{ s}^{-1}$ (middle panel) and $f = 1 \times 10^{-3} \text{ s}^{-1}$ (bottom panel).

upwelling motions inside them (notice that the negative ω represents upwelling), and these anticyclones are cloudier than surroundings. The vortex-size upwellings in anticyclones provide strong upward transport of tracers as shown in the right panel. At the meantime, smaller-scale waves and filaments around vortices have strong vertical motions as well, and they significantly contribute to *local* vertical transport. However, these small-scale transport are in both directions which might tend to cancel out each other, and it is unclear, by just reading the maps shown in Figure 8, how much they contribute to the *total* vertical transport.

To better quantify contributions of flows with different horizontal lengthscales to the total vertical tracer transport, as a standard exercise in meteorology, we calculate the cospectral power density for the quantity $\omega'q'$, which is simply $2\Re(q_k \omega_k^*)$ where q_k and ω_k are the coefficients at wavenumber k space for tracer and vertical velocity, and ω_k^* is the conjugate of ω_k (e.g., Randel & Held 1991). Figure 9 shows the cospectral power density at a pressure of 0.43 bar (right above the condensation level), for simulations with $f = 0$ to $f = 1 \times 10^{-3} \text{ s}^{-1}$ but all with a fixed domain size in the upper panel.

When $f = 0$ or the vortex scale is comparable to the simulated domain size, the divergent and convergent flow occurs mostly on the domain scale, and therefore the dominant transport power is at the lowest wavenumbers. As f increases, similar to the KE spectra, the peak of the $\omega'q'$ cospectral power density is at lengthscales close to the deformation radius and systematically shifts to larger wavenumber (smaller lengthscale). The peak value of the cospectral power

density also monotonically decreases with increasing f , consistent with the weakened transport of tracers shown in Figure 7.

The dashed lines in the lower panel of Figure 9 show spectra of three additional models with extended domain sizes for $f = 1 \times 10^{-4}, 2 \times 10^{-4}$ and $3 \times 10^{-4} \text{ s}^{-1}$. Cases with $f \geq 4 \times 10^{-4} \text{ s}^{-1}$ and with the original domain size are also plotted in the same panel. Models with $f \leq 2 \times 10^{-4} \text{ s}^{-1}$ no longer show peaks at the largest lengthscale. Instead, the dominant transport mode is well correlated with rotation even at small f when the vortices are no longer limited by the domain size. The $\omega'q'$ spectra of all these models peak at lengthscales close to the deformation radius, and the peak values also monotonically decrease with increasing f .

At lower pressures, however, the vertical transport by smaller-scale motions (those associated with inertia gravity waves and filaments) start to be comparable or even dominate over that by motions at lengthscales near the deformation radius. Figure 10 shows the $\omega'q'$ cospectral power density at different pressure levels for the simulation with $f = 0$ in the top panel, with $f = 4 \times 10^{-4} \text{ s}^{-1}$ in the middle panel and with $f = 1 \times 10^{-3} \text{ s}^{-1}$ in the bottom panel. In the lower two panels, at lower pressures, the cospectra starts to split into two groups, one being the motions near the deformation radius and the other being at much smaller lengthscales. The total transport power by the small-scale groups is comparable to or larger than that by the vortex-scale motions at lower pressures.

There is likely a dynamical reason for this transition. As discussed in Section 3.1.2, tracer transport by a thermally-driven circulation requires that rising air is heated and subsiding air cools. This works well in the non-rotating cases, which is why tracer transport is always dominated by the lowest wavenumber at all pressure levels in the case with $f = 0$ (top panel of Figure 10). For large f , the thermally-driven transport works well only when the air in the ascending cloudy regions is not cooler than air in the descending cloudless regions. For example, in the case with $f = 4 \times 10^{-4} \text{ s}^{-1}$, the temperature in cloudy regions is generally lower than that in cloudless regions when the pressure is less than 0.17 bar. In the middle panel of Figure 10 with $f = 4 \times 10^{-4} \text{ s}^{-1}$, the total transport power by smaller scales starts to be comparable to that by the vortex-scale motions at 0.17 bar. At an even lower pressure, because the direct thermal-driven circulation is likely limited due to thermodynamic constraints, eddy-driven (here the eddy refers to flows with lengthscale smaller than the dominant vortex scale) circulation becomes increasingly important in the vertical tracer transport mechanism.

3.4 Dynamics with varying bottom drag

Kinetic energy of the flow at lengthscales larger than the deformation radius is strongly dissipated by the frictional drag that extends from bottom up to 5 bars. Why do flows driven by the cloud formation well above 5 bars experience bottom drag? In quasi-geostrophic turbulence, if KE is injected from the baroclinic flow (which refers to structures with vertical variation), the upscale transfer of KE also occurs over the vertical direction in the horizontal scale close to the deformation radius (e.g., Rhines 1977; Salmon 1978, 1980; Smith & Vallis 2002; Chemke & Kaspi 2015). KE associated with the baroclinic flow will be transferred towards flows with greater vertical wavelength, and eventually to the barotropic flow (which refers to flows independent of pressure or height). KE associated with the barotropic flow then continues to transfer to larger horizontal lengthscales. In our case, KE is injected by the baroclinic cloud-radiative-driven dynamics. When it is transferred towards the barotropic flow, the KE is deposited mostly in the deep layer simply because there is more mass there. With a strong bottom drag that directly removes KE

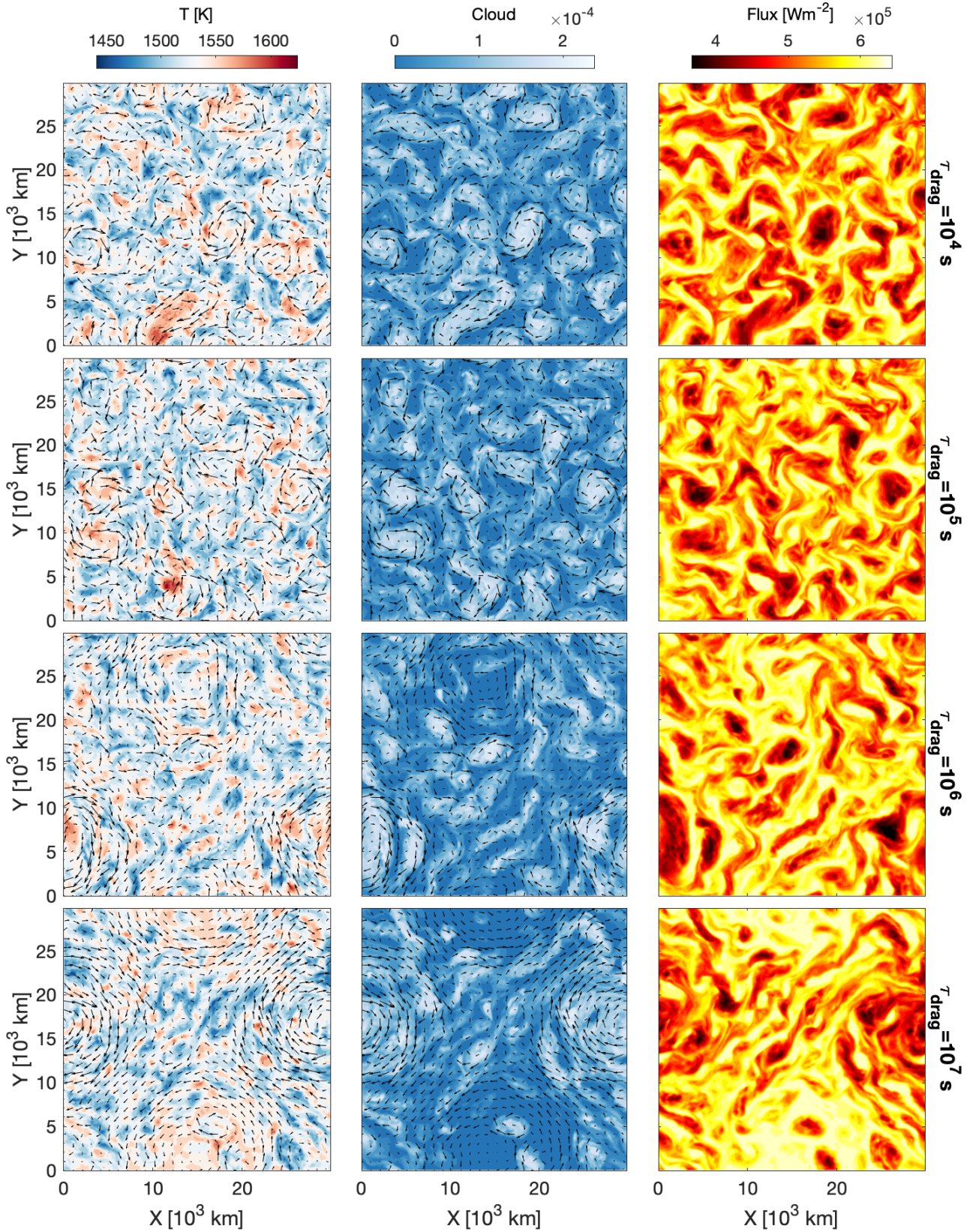


Figure 11. Instantaneous horizontal cloud mixing ratio at 0.23 bar in the left column, the corresponding temperature at 0.23 bar in the middle column, and the corresponding outgoing top-of-atmosphere thermal flux in the right column. Arrows represent horizontal wind vectors. These are results from models with different bottom frictional drag $\tau_{\text{drag}} = 10^4$ s (top row), 10^5 s (second row), 10^6 s (third row) and 10^7 s (bottom row). The Coriolis parameter is $f = 1 \times 10^{-3} \text{ s}^{-1}$ for all models. All other parameters are the same among these models.

of the deep layers, the rate of KE generation from the upper cloud level is not sufficient to maintain a strong barotropic flow. Therefore, in Figure 5, the strength of the domain-scale flow associated with the barotropic flows at 0.23 bar is rather weak.

To investigate the turbulence properties when the damping on the barotropic flow is different, we performed additional experiments assuming different bottom drag timescales of $\tau_{\text{drag}} = 10^4, 10^6$ and 10^7 s. This is also motivated by the fact that the bottom drag only rather crudely represents the effect of mixing with the deep interior. There is no justification for how strong the drag should be, and here we test the sensitivity of our results to the varying drag timescale. We assume $f = 1 \times 10^{-3} \text{ s}^{-1}$ in order to maximize scale separation between the deformation radius and domain size. Results are shown in Figure 11, in which temperature maps at 0.23 bar are shown on the left column, maps of cloud mixing ratio are shown at 0.23 bar on the middle column, and the outgoing radiative flux is shown on the right column. The drag timescales from the top to bottom row are $10^4, 10^5, 10^6$ and 10^7 s, respectively. Results with $\tau_{\text{drag}} = 10^4$ and 10^5 s appear to be very similar in terms of the typical storm sizes, amplitudes of temperature perturbations and cloud mixing ratio. With strong drags, storms and vortices are mostly in sizes close to the deformation radius. When $\tau_{\text{drag}} = 10^7$ s, there appears to be two dominant horizontal modes of vortices, one being those with sizes close to the deformation radius and the other being a pair of much larger, domain-size cyclone and anticyclone. The two distinctive modes can also be easily seen in the cloud mixing ratio and the outgoing thermal flux maps (the bottom row in Figure 11). Unlike the small vortices close to the deformation radius, the domain-size vortices are dominated by a pressure-independent component.

We perform spectral analysis to quantify the scale separation of the vortices. Figure 12 shows the same quantities in spectral space as in Figure 5 but for the four different τ_{drag} . In the KE spectra, both cases with $\tau_{\text{drag}} = 10^4$ and 10^5 show a single peak at $1.2 \times 10^{-6} \text{ rad m}^{-1}$, and then the KE decreases at both longer and shorter wavelengths. At smaller wavelengths (larger lengthscales), the case with $\tau_{\text{drag}} = 10^4$ s shows a lower energy density than that with $\tau_{\text{drag}} = 10^5$ s. With longer τ_{drag} , the KE spectra show two peaks, one at $1.2 \times 10^{-6} \text{ rad m}^{-1}$ and a stronger one at the smallest wavenumber (the domain size). The KE spectra at wavenumbers larger than $3 \times 10^{-6} \text{ rad m}^{-1}$ are similar among the four cases. The local peak of KE spectral density near $1.2 \times 10^{-6} \text{ rad m}^{-1}$ in cases with larger τ_{drag} is smaller than that with smaller τ_{drag} . Similarly, spectra of q'^2 , T'^2 and F'^2 are all affected by the increasing τ_{drag} .

As the bottom frictional drag becomes weaker, the rate at which it dissipates KE decreases, and the KE associated with the barotropic flow accumulates. Dynamics of the nearly barotropic flows are more akin to the 2D flow, and its KE in the f -plane can be transferred to the domain scale if the dissipation is weak. Indeed, the simulation with $\tau_{\text{drag}} = 10^7$ s shows a pair of cyclone and anticyclone comparable to the domain size. They appear as a pair because of angular momentum conservation. After the vortices grow to the domain size, they cease to grow in size but their KE increases until an equilibrium between the KE upscale transfer and removal by the drag is reached. In this situation, the KE power spectrum steepens towards the largest scale.

The domain-scale vortices exert feedbacks to the formation of storms on scales close to the deformation radius. The first prominent feature in Figure 11 is the existence of domain-scale isobaric temperature difference, cloud patterns and outgoing thermal flux. The domain-scale cyclone is slightly cooler, less cloudy and emits more flux to the space, whereas the anticyclone is the opposite. Unlike cloud formation with sizes near the deformation radius, these

domain-size structure is not directly driven by the geostrophic adjustment. Effects of the bottom frictional drag—analogue to Ekman pumping and suction—acts against this configuration. For the nearly barotropic flow, the pressure gradient is mainly balanced by the Coriolis force associated with the wind in the absence of drag. In the presence of frictional forces, the three-way force balance induces a drift in the direction from high pressure to low pressure—this means a convergent bottom flow that pushes air upward in the cyclone and divergent flow that sucks air downward in the anticyclone. This effect should in principle promote domain-scale cloud formation in the cyclone and suppress cloud formation in the anticyclone, which is the opposite to our results. The responsible mechanism is likely the migration of vortex under inhomogeneous background vorticity. Vortices tend to migrate to regions where the background vorticity matches the vortex's absolute vorticity. An important example is the migration of vortices under the planetary vorticity gradient—cyclones migrate poleward and anticyclones migrate equatorward (e.g., Adem 1956; LeBeau Jr & Dowling 1998; Scott 2011). In our model with $\tau_{\text{drag}} = 10^7$ s, the magnitude of relative vorticity anomalies associated with the domain-size vortices is comparable to f , and therefore the background vorticity is no longer homogeneous. Cloudless cyclones have relatively high absolute vorticity and cloudy anticyclones have relatively low absolute vorticity. When small cyclones are generated inside the domain-size anticyclone which has low absolute vorticity, they tend to migrate to regions with high absolute vorticity—the domain-size cyclone. Whereas cloud-forming anticyclones tend to move to the domain-size anticyclone. Overtime, clouds tend to accumulate in the domain-size anticyclonic region and the domain-size cyclonic region is filled with cloudless air.⁷

Secondly, the strong shear flows associated with the strong domain-size vortices decrease the efficiency of cloud formation. Newly formed storms near the strong shear regions are sometimes disrupted and sheared apart before they become mature. This likely causes smaller peaks around the internal deformation radius in the KE power spectra for models with $\tau_{\text{drag}} = 10^6$ and 10^7 s than in those with $\tau_{\text{drag}} = 10^4$ and 10^5 s (see Figure 12).

Clouds induce radiative heating to the domain-scale anticyclonic region, whilst relatively cloud-free air cools the domain-scale cyclonic region. This drives upwelling in the anticyclonic region and downwelling in the cyclonic region, providing extra tracer transport in addition to the vortex migration. As a result of cloud radiative feedback, the domain-scale vortices have temperature variations on isobars. This effect is prominent in the case with $\tau_{\text{drag}} = 10^7$ s. This is dynamically interesting because, by definition, the barotropic flow is independent of pressure (or height). Given that the bottom temperature is almost horizontally uniform in our model, a “true” barotropic flow should not have isobaric temperature variation at any pressure. In our case, the large, domain-size vortices is only quasi-barotropic due to the cloud radiative feedback.

In a short summary, the strength of the nearly barotropic mode is sensitive to the strength of the bottom drag. In the strong drag case, the nearly barotropic mode is efficiently damped by the drag, and dynamics in the cloud forming region is dominated by the baroclinic, cloud forming vortices with sizes close to the deformation radius. In

⁷ We show a movie of the cloud mixing ratio at 0.32 bar (available at <https://youtu.be/8e4wH63bFsg>) and a movie of the potential vorticity at 0.32 bar (available at <https://youtu.be/TBRuh2mdWo8>) for the model with $\tau_{\text{drag}} = 10^7$ s. The relative migration between the small vortices with sizes close to the deformation radius and the large, domain-size vortices are easily visualized in these movies.

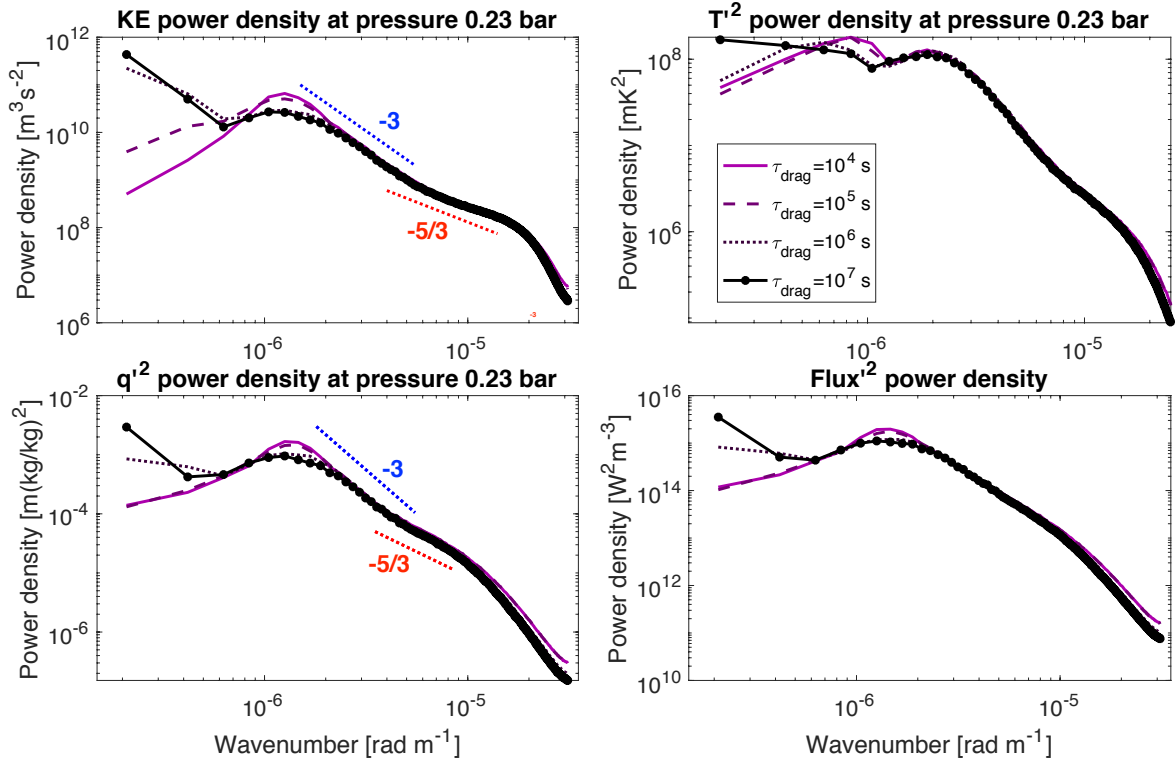


Figure 12. Similar to Figure 5 but shows power spectra of KE, T^2 , q^2 and F^2 for simulations with different bottom frictional drag $\tau_{\text{drag}} = 10^4$ s, 10^5 s, 10^6 s and 10^7 s and a fixed Coriolis parameter $f = 1 \times 10^{-3} \text{ s}^{-1}$.

the weak drag case, the nearly barotropic mode takes kinetic energy from baroclinic modes and is able to grow, such that it can affect dynamics at the cloud forming levels as seen in Figure 11.

4 DISCUSSION

4.1 Observational implications

Most observed lightcurve variability of BDs and free-floating EGPs are thought to be caused by rotational modulation of surface inhomogeneity (Biller 2017; Artigau 2018). The variability often appears to be periodic, indicating the presence of quasi-stationary surface features. However, a fraction of the variability exhibits changes over short timescales comparable to the rotation period, suggesting that the surface features evolve over short timescales (Artigau et al. 2009; Wilson et al. 2014; Metchev et al. 2015; Apai et al. 2017). A small fraction of them even show long-period (over 20 hours), non-sinusoidal variability (Metchev et al. 2015), and it is unclear whether rotational modulation is the typical cause. The stochastic evolution of storms driven by cloud radiative feedback may help to explain these irregularities in the lightcurve variability. Figure 13 shows the domain-averaged outgoing thermal flux as a function of time for three simulations with $\tau_{\text{drag}} = 10^5$ s and $f = 2 \times 10^{-4}$, 4×10^{-4} and $8 \times 10^{-4} \text{ s}^{-1}$, and for a simulation with $\tau_{\text{drag}} = 10^7$ s and $f = 1 \times 10^{-3} \text{ s}^{-1}$. The variability in these simulations are solely caused by the statistical fluctuation of the storm system. The case with $f = 2 \times 10^{-4} \text{ s}^{-1}$ exhibits the largest fractional flux variability up to about 7% peak-to-peak variation, while that with $8 \times 10^{-4} \text{ s}^{-1}$ is the smallest among these three cases (about 2% peak-to-peak vari-

ation). Although the case with $\tau_{\text{drag}} = 10^7$ s and $f = 1 \times 10^{-3} \text{ s}^{-1}$ develops domain-size vortices (see Section 3.4), the amplitude of its resulting lightcurve variability is not obviously larger than that of other cases shown in Figure 13. The typical evolution timescale of the flux is tens of hours, longer than the overturning timescale of an individual storm (which can be roughly estimated as on the order of $\sim 10^4$ s from the dominant lengthscales and wind speed of the storms). Figure 13 suggests that the more storms in the domain, the less effect that the fluctuation of a single storm would have in the total flux variability.

In the planetary surface, the latitudinal-dependence of the Coriolis parameter f indicates latitudinal-dependent sizes of local storms. Near the equator where f is small, storms might be able to grow to a lengthscale that is a nontrivial fraction of the planetary radius. For example, a BD with a 5-hour rotation has a Coriolis parameter at $f = 1.2 \times 10^{-4} \text{ s}^{-1}$ at 10° latitude and $f = 7 \times 10^{-4} \text{ s}^{-1}$ at the pole. Given our model conditions, this results in a typical storm diameter of about 1.8×10^4 km at 10° latitude and 3×10^3 km on the poles. Assuming a Jupiter radius, a single storm near the pole covers less than $\sim 0.1\%$ of the disk whereas that at 10° latitude covers $\sim 1.7\%$ of the disk. If the BD or the directly imaged EGP is observed pole on, statistical fluctuation of storms is expected to cause negligible flux variability. However, if the view equator on, not only rotational modulation is maximized, but the evolution of the larger storms may induce additional variability over a timescale on the order of tens of hours. This may contribute to the irregular variability of many observed lightcurves of BDs (e.g., Metchev et al. 2015).

When vertical transport of clouds is dominated by large-scale flows via cloud radiative feedback, one would expect that clouds are thicker at low latitudes and thinner at high latitudes for a BD with certain

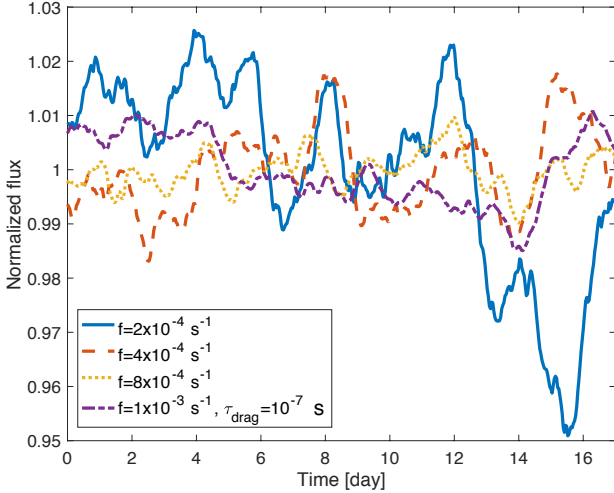


Figure 13. Normalized domain-averaged outgoing thermal flux as a function of time for three simulations with $\tau_{\text{drag}} = 10^5$ s and $f = 2 \times 10^{-4}$, 4×10^{-4} and 8×10^{-4} s $^{-1}$ (corresponding to f at polar regions of objects with rotation periods of 17.5, 8.7 and 4.4 hours, respectively), and for a simulation with $\tau_{\text{drag}} = 10^7$ s and $f = 1 \times 10^{-3}$ s $^{-1}$ (corresponding to f at the polar region of an object with a rotation period of 3.5 hours). All models are in a fixed domain size of 30000 km \times 30000 km. The lightcurves are normalized relative to their time-mean values.

rotation rate. If the BD rotates sufficiently slow, the equator-to-pole cloud thickness variation may be small. Under similar atmospheric conditions — including temperature, gravity and metallicity, BDs that rotate faster are expected to have overall thinner clouds than those rotate slower. These consequences have implications for observed near-IR colors for BDs and directly imaged EGPs as the thickness of clouds affects the spectral properties. For example, different overall cloud thickness caused by different rotation rate may contribute to the near-IR color scattering of mid-to-late L dwarfs (e.g., Faherty et al. 2016). Recently, Vos et al. (2017) and Vos et al. (2020) suggested that BDs that are viewed from more equator-on tend to exhibit redder near-IR colors and larger flux variability than those viewed more pole-on, for which our numerical results naturally support.

4.2 Unresolved issues and outlook

We have shown in Figure 7 that cloud thickness decreases with increasing rotation rate. One would intuitively expect that faster rotation can lead to a more stringent balanced state of the flow given roughly the same amount of cloud radiative feedback, and therefore weaker vertical motions to transport tracers against particle settling. However, this picture itself would *not* automatically imply a mechanism. This is a central unresolved issue of this study. Revealing the detailed mechanism likely requires an understanding of the eddies and their effect on the mean flows (here, eddies refer to motions with scales smaller than the vortex scale, and the mean flows refer to the vortex motions). If the vortex is roughly circular, the flow can be decomposed into axisymmetric and non-axisymmetric components. The axisymmetric flow will be largely in balance between the pressure gradient force and the Coriolis force (plus the centrifugal force if it is important), with a residual component providing divergence and convergence of the vortex that are essential to drive cloud formation. The balance of the residual overturning circulation is primarily be-

tween angular momentum transport by eddies and the Coriolis force associated with the residual overturning flow if the vortex is close to quasi-geostrophic balance (e.g., Showman & Kaspi 2013). Therefore, the cloud-forming overturning circulation is essentially both thermally driven and eddy regulated. Furthermore, near the cloud top, as we have shown in Figure 10, eddies contribute significantly to the net upward transport of clouds. Cloud vertical transport near the cloud top is essential because the cloud-top pressure determines the outgoing thermal flux and therefore the strength of the atmospheric heating. In summary, understanding eddies is essential to pin down the mechanism by which stronger rotation leads to vertically thinner clouds. Future models adopting various level of complexity are needed to investigate this mechanism.

Our models show sensitivity to the strength of prescribed bottom frictional drag. This is because kinetic energy generated in the cloud forming region (which lies well above the region where drag is applied) can be transferred to deeper layers, forming dynamical modes that tend to be pressure independent and with horizontal lengthscales larger than the deformation radius. The strength of this mode is sensitive to the rate of energy removed by the bottom drag (see results and discussion in Section 3.4). This highlights the fact that conditions in layers deeper than the observable layers may influence observable flow and cloud properties. The form and strength of the drag are highly uncertain due to the unknown nature of interactions between the interior and the simulated shallow outer layer. To date, no systematic theoretical study provides a guidance as to how such interactions should be parameterized in shallow models. The uncertainties in the bottom boundary conditions and the impacts on the general circulation have long been an issue for shallow models of gaseous planets (e.g., Showman et al. 2020). Such issues have been shown for shallow models relevant to Jupiter (e.g., Schneider & Liu 2009) and to hot Jupiters (e.g., Mayne et al. 2017; Sainsbury-Martinez et al. 2019; Carone et al. 2020).

Our idealized models are dedicated to a clear understanding of dynamical mechanisms. An obvious next step within this framework is to extend the model domain to a global geometry which includes effects of the latitudinal variation of f —the so-called β effect where $\beta = df/dy$. The β effect plays a central role in driving zonal banding and jets in Jovian and Saturnian atmospheres (see reviews by, for example, Vasavada & Showman 2005; Showman et al. 2018). This would help to clarify whether BDs and directly EGPs exhibit zonal jets like Jupiter and Saturn as indicated by long-term lightcurve monitoring (Apai et al. 2017) and simultaneous tracking of radio and near-IR flux variability (Allers et al. 2020). Global models are also necessary to assess whether circulation driven by cloud radiative feedback can quantitatively explain the observed lightcurve variability of BDs. Future developments beyond the current idealized framework include adopting a realistic radiative transfer scheme coupled to realistic chemistry and cloud formation—this allows direct comparisons between global models and the rich observed spectrum, near-IR colors and spectral time variability of BDs and directly EGPs.

An alternative scenario associated with thermo-chemical effects of CO/CH₄ and N₂/NH₃ conversion has been proposed to explain L dwarf spectrum and the L/T transition using static, 1D radiative-convective equilibrium framework (Tremblin et al. 2016, 2019). In our dynamical framework, cloud is chosen as a key dynamically active tracer for its excessive opacity in typical L and early T dwarfs (Marley & Robinson 2015). When the chemical conversion timescale is close to or longer than dynamical timescales, the potential correlation between horizontal distribution of chemical species (therefore their radiative feedback) and large-scale dynamics may play a similar role as a dynamically active tracer, contributing to

the heating/cooling rates that shape the circulation. Such radiative feedback by chemical quenching on the general circulation has been investigated for hot Jupiters (e.g., [Steinrueck et al. 2019](#); [Drummond et al. 2020](#)), and will be an interesting topic in future studies for BDs and directly imaged EGPs.

5 CONCLUSIONS

Cloud radiative feedback may play an essential role in driving vigorous circulation in atmospheres of self-luminous, substellar objects including brown dwarfs (BDs) and directly imaged extrasolar giant planets (EGPs). In this study, we have numerically investigated the atmospheric circulation in conditions relevant to these objects using a general circulation model that is self-consistently coupled with idealized cloud formation and its radiative feedback. As a first step in this line of study and to better understand the effects of rotation on the turbulent cloud formation, our models adopt a constant Coriolis parameter f across a Cartesian domain and with a double-periodic horizontal boundary condition. We have reached the following key conclusions:

- Vigorous atmospheric circulation can be triggered and self-sustained by cloud radiative feedback in conditions appropriate for BDs and directly imaged EGPs. In a constant- f approximation, the circulation is dominated by turbulent vortices, with thick clouds forming in the anticyclones and thin clouds or clear sky in the cyclones. Horizontally averaged wind speed can be several hundred m s^{-1} with local wind speeds exceeding 1000 m s^{-1} , and isobaric temperature differences can be over 100 K for plausible physical parameters. Fractional outgoing thermal flux differences between cloudy and cloudless regions can be comparable to 1. This is a natural and robust mechanism to generate significant surface inhomogeneity that is responsible for the observed lightcurve variability of BDs and EGPs.
- In the presence of strong rotation and strong deep frictional drag (which crudely represents interactions between the weather layer and the deep quiescent interior), the characteristic horizontal lengthscales of dominant vortices are close to the deformation radius $L_d = c_g/f$ where c_g is the phase speed of gravity waves. In the absence of rotation or when rotation is weak, the circulation is characterized by convergent and divergent flows with horizontal lengthscales regulated by the radiative timescale of the atmosphere.
- Stronger rotation leads to vertically thinner clouds, and the cloud thickness is greatest in the absence of rotation. Both the vortex-scale flow and smaller-scale inertia gravity waves contribute to the vertical transport of vapor and clouds. The mechanism by which rotation regulates the cloud thickness is likely related to interactions between vortices and smaller-scale flows.
- When the deep frictional drag is weak, there can be two distinctive modes of vortices. The first mode has a typical horizontal lengthscale close to the deformation radius and is driven directly by the geostrophic adjustment associated with cloud radiative feedback. The other mode has a strong pressure-independent component and can grow to a horizontal lengthscale comparable to the simulated domain size. The large, domain-scale vortices could affect efficiency of cloud formation and induce horizontal drifts of cloud-forming vortices with a size close to the deformation radius.
- Storms driven by cloud radiative feedback evolve over timescales of several to tens of hours, and the statistical fluctuation of the ensemble of storms could induce variability of the domain-mean flux. Such flux variability may help to explain the irregular lightcurve variability observed in a fraction of BDs. The change of

cloud thickness with different Coriolis parameter f indicates that the cloud thickness may be different at different latitudes of the BDs or directly imaged EGPs. The global-mean cloud thickness might also be different for objects with different rotation rate. These may contribute to the observed scattered near-IR colors of dusty L dwarfs and the viewing angle dependent near-IR colors of BDs.

ACKNOWLEDGEMENTS

We thank Ray Pierrehumbert and Yifan Zhou for helpful discussion and Tad Komacek for comments on the draft. X.T. acknowledges support from the European community through the ERC advanced grant EXOCONDENSE (PI: R.T. Pierrehumbert). This work was completed with resources provided by the department of Physics at University of Oxford and the Lunar and Planetary Laboratory at University of Arizona.

DATA AVAILABILITY

The data underlying this article will be shared on reasonable request to the corresponding author.

REFERENCES

- Ackerman A. S., Marley M. S., 2001, *ApJ*, **556**, 872
- Adcroft A., Campin J.-M., Hill C., Marshall J., 2004, *Monthly Weather Review*, **132**, 2845
- Adem J., 1956, *Tellus*, **8**, 364
- Allard F., Hauschildt P. H., Alexander D. R., Tamanai A., Schweitzer A., 2001, *The Astrophysical Journal*, **556**, 357
- Allers K. N., Vos J. M., Biller B. A., Williams P. K., 2020, *Science*, **368**, 169
- Andrews D. G., Holton J. R., Leovy C. B., 1987, *Middle atmosphere dynamics*. Vol. 40, Academic press
- Apai D., Radigan J., Buenzli E., Burrows A., Reid I. N., Jayawardhana R., 2013, *ApJ*, **768**, 121
- Apai D., et al., 2016, *ApJ*, **820**, 40
- Apai D., et al., 2017, *Science*, **357**, 683
- Arbic B. K., Flierl G. R., 2003, *Physics of Fluids*, **15**, 2177
- Arbic B. K., Flierl G. R., Scott R. B., 2007, *Journal of physical oceanography*, **37**, 1470
- Artigau É., 2018, preprint, ([arXiv:1803.07672](#))
- Artigau É., Bouchard S., Doyon R., Lafrenière D., 2009, *The Astrophysical Journal*, **701**, 1534
- Barman T. S., Macintosh B., Konopacky Q. M., Marois C., 2011a, *ApJ*, **733**, 65
- Barman T. S., Macintosh B., Konopacky Q. M., Marois C., 2011b, *ApJ*, **735**, L39
- Biller B., 2017, *Astronomical Review*, **13**, 1
- Biller B. A., et al., 2015, *The Astrophysical Journal Letters*, **813**, L23
- Biller B. A., et al., 2018, *AJ*, **155**, 95
- Bowler B. P., Zhou Y., Morley C. V., Kataria T., Bryan M. L., Benneke B., Batygin K., 2020, *ApJ*, **893**, L30
- Bryan M. L., Benneke B., Knutson H. A., Batygin K., Bowler B. P., 2018, *Nature Astronomy*, **2**, 138
- Buenzli E., et al., 2012, *ApJ*, **760**, L31
- Buenzli E., Apai D., Radigan J., Reid I. N., Flateau D., 2014, *The Astrophysical Journal*, **782**, 77
- Burgasser A. J., Marley M. S., Ackerman A. S., Saumon D., Lodders K., Dahn C. C., Harris H. C., Kirkpatrick J. D., 2002, *The Astrophysical Journal Letters*, **571**, L151
- Burningham B., Marley M. S., Line M. R., Lupu R., Visscher C., Morley C., Saumon D., Freedman R., 2017, *Monthly Notices of the Royal Astronomical Society*, p. stx1246

- Burrows A., Sudarsky D., Hubeny I., 2006, *ApJ*, **640**, 1063
- Carone L., et al., 2020, *Monthly Notices of the Royal Astronomical Society*, **496**, 3582
- Chabrier G., Baraffe I., Allard F., Hauschildt P., 2000, *The Astrophysical Journal*, **542**, 464
- Charnay B., BÄ@zard B., Baudino J.-L., Bonnefoy M., Boccaletti A., Galicher R., 2018, *The Astrophysical Journal*, **854**, 172
- Charney J. G., 1963, *Journal of the Atmospheric Sciences*, **20**, 607
- Charney J. G., 1971, *Journal of the Atmospheric Sciences*, **28**, 1087
- Chauvin G., et al., 2017, *Astronomy & Astrophysics*, **605**, L9
- Chemke R., Kaspi Y., 2015, *Journal of the Atmospheric Sciences*, **72**, 3891
- Collins W. D., et al., 2004, *Description of the NCAR community atmosphere model (CAM 3.0)*
- Crossfield I. J. M., et al., 2014, *Nature*, **505**, 654
- Currie T., et al., 2011, *The Astrophysical Journal*, **729**, 128
- De Verdiere A. C., 1980, *Geophysical & Astrophysical Fluid Dynamics*, **15**, 213
- Dewan E. M., 1979, *Science*, **204**, 832
- Drummond B., et al., 2020, *Astronomy & Astrophysics*, **636**, A68
- Emanuel K. A., 1986, *Journal of the Atmospheric Sciences*, **43**, 585
- Eriksson S. C., Janson M., Calissendorff P., 2019, *Astronomy & Astrophysics*, **629**, A145
- Faherty J. K., et al., 2016, *The Astrophysical Journal Supplement Series*, **225**, 10
- Freedman R. S., Lustig-Yaeger J., Fortney J. J., Lupu R. E., Marley M. S., Lodders K., 2014, *The Astrophysical Journal Supplement Series*, **214**, 25
- Freytag B., Allard F., Ludwig H.-G., Homeier D., Steffen M., 2010, *A&A*, **513**, A19
- Gierasch P. J., Ingersoll A. P., Williams R. T., 1973, *Icarus*, **19**, 473
- Gill A., Donn W., 2016, *Atmosphere—Ocean Dynamics*. Elsevier Science, <https://books.google.co.uk/books?id=lypfDAAAQBAJ>
- Guillot T., 2010, *A&A*, **520**, A27
- Held I. M., Zhao M., 2008, *Journal of the atmospheric sciences*, **65**, 2003
- Helling C., 2019, *Annual Review of Earth and Planetary Sciences*, **47**, 583
- Helling C., Casewell S., 2014, *The Astronomy and Astrophysics Review*, **22**, 1
- Helling C., Fomins A., 2013, *Philosophical Transactions of the Royal Society of London A: Mathematical, Physical and Engineering Sciences*, **371**, 20110581
- Helling C., et al., 2008, *Monthly Notices of the Royal Astronomical Society*, **391**, 1854
- Hitchcock J. A., et al., 2020, arXiv e-prints, [p. arXiv:2005.06906](https://arxiv.org/abs/2005.06906)
- Holton J. R., 1986, *Journal of Geophysical Research: Atmospheres*, **91**, 2681
- Holton J. R., Hakim G. J., 2012, *An introduction to dynamic meteorology*. Vol. 88, Academic press
- Ingraham P., et al., 2014, *ApJ*, **794**, L15
- Jäger C., Dorschner J., Mutschke H., Posch T., Henning T., 2003, *Astronomy & Astrophysics*, **408**, 193
- Kirkpatrick J. D., et al., 2012, *The Astrophysical Journal*, **753**, 156
- Knapp G., et al., 2004, *The Astronomical Journal*, **127**, 3553
- Komacek T. D., Showman A. P., 2016, *The Astrophysical Journal*, **821**, 16
- Komacek T. D., Showman A. P., Parmentier V., 2019, *The Astrophysical Journal*, **881**, 152
- Kuo A. C., Polvani L. M., 1997, *Journal of Physical Oceanography*, **27**, 1614
- Kylling A., Stamnes K., Tsay S.-C., 1995, *Journal of Atmospheric Chemistry*, **21**, 115
- LeBeau Jr R., Dowling T., 1998, *Icarus*, **132**, 239
- Leggett S. K., Tremblin P., Saumon D., Marley M. S., Morley C. V., Amundsen D. S., Baraffe I., Chabrier G., 2016a, *The Astrophysical Journal*, **824**, 2
- Leggett S. K., et al., 2016b, *ApJ*, **830**, 141
- Leggett S., et al., 2019, *The Astrophysical Journal*, **882**, 117
- Lew B. W., et al., 2016, *The Astrophysical Journal Letters*, **829**, L32
- Lew B. W., et al., 2020, *The Astronomical Journal*, **159**, 125
- Lindborg E., 1999, *Journal of Fluid Mechanics*, **388**, 259
- Lindborg E., 2007, *Journal of the atmospheric sciences*, **64**, 1017
- Liu B., Showman A. P., 2013, *ApJ*, **770**, 42
- Manjavacas E., et al., 2017, *The Astronomical Journal*, **155**, 11
- Manjavacas E., et al., 2019, *The Astrophysical Journal Letters*, **875**, L15
- Marley M. S., Robinson T. D., 2015, *Annual Review of Astronomy and Astrophysics*, **53**, 279
- Marley M. S., Saumon D., Goldblatt C., 2010, *ApJ*, **723**, L117
- Marley M. S., Saumon D., Cushing M., Ackerman A. S., Fortney J. J., Freedman R., 2012, *ApJ*, **754**, 135
- Mayne N. J., et al., 2017, *Astronomy & Astrophysics*, **604**, A79
- McWILLIAMS J. C., Weiss J. B., Yavneh I., 1999, *Journal of Fluid Mechanics*, **401**, 1
- Metchev S. A., et al., 2015, *ApJ*, **799**, 154
- Miles-Páez P. A., Pallé E., Zapatero Osorio M. R., 2017, *MNRAS*, **472**, 2297
- Miles-Páez P. A., et al., 2019, *The Astrophysical Journal*, **883**, 181
- Miles B. E., et al., 2020, arXiv e-prints, [p. arXiv:2004.10770](https://arxiv.org/abs/2004.10770)
- Millar-Blanchaer M. A., et al., 2020, *The Astrophysical Journal*, **894**, 42
- Morley C. V., Fortney J. J., Marley M. S., Visscher C., Saumon D., Leggett S., 2012, *The Astrophysical Journal*, **756**, 172
- Moses J. I., et al., 2016, *ApJ*, **829**, 66
- Nastrom G., Gage K., Jasperson W., 1984, *Nature*, **310**, 36
- Oppenheimer B. R., et al., 2013, *ApJ*, **768**, 24
- Parmentier V., Showman A. P., Lian Y., 2013, *Astronomy & Astrophysics*, **558**, A91
- Pierrehumbert R. T., 2010, *Principles of planetary climate*. Cambridge University Press
- Radigan J., Jayawardhana R., Lafrenière D., Artigau É., Marley M., Saumon D., 2012, *ApJ*, **750**, 105
- Rajan A., et al., 2015, *Monthly Notices of the Royal Astronomical Society*, **448**, 3775
- Randel W. J., Held I. M., 1991, *Journal of the atmospheric sciences*, **48**, 688
- Reinaud J. N., Dritschel D. G., 2019, *Journal of Fluid Mechanics*, **863**, 60
- Reiners A., Basri G., 2008, *ApJ*, **684**, 1390
- Rennó N. O., Ingersoll A. P., 1996, *Journal of the Atmospheric Sciences*, **53**, 572
- Rhines P. B., 1975, *Journal of Fluid Mechanics*, **69**, 417
- Rhines P. B., 1977, in *Vol. 6: Marine Modeling, The Sea*. Wiley and Sons, pp 189–318
- Sainsbury-Martinez F., et al., 2019, *Astronomy & Astrophysics*, **632**, A114
- Salmon R., 1978, *Geophysical & Astrophysical Fluid Dynamics*, **10**, 25
- Salmon R., 1980, *Geophysical & Astrophysical Fluid Dynamics*, **15**, 167
- Saumon D., Marley M. S., 2008, *The Astrophysical Journal*, **689**, 1327
- Saumon D., Marley M. S., Cushing M. C., Leggett S. K., Roellig T. L., Lodders K., Freedman R. S., 2006, *ApJ*, **647**, 552
- Schäfer J., Lee S.-C., Kienle A., 2012, *Journal of Quantitative Spectroscopy and Radiative Transfer*, **113**, 2113
- Schneider T., Liu J., 2009, *Journal of Atmospheric Sciences*, **66**, 579
- Schneider A. C., Hardegree-Ullman K. K., Cushing M. C., Kirkpatrick J. D., Shkolnik E. L., 2018, *The Astronomical Journal*, **155**, 238
- Scott R., 2011, *Geophysical & Astrophysical Fluid Dynamics*, **105**, 409
- Shapiro R., 1970, *Reviews of geophysics*, **8**, 359
- Showman A. P., Kaspi Y., 2013, *ApJ*, **776**, 85
- Showman A., Ingersoll A., Achterberg R., Kaspi Y., 2018, *Saturn in the 21st Century* (Baines, K. and Flasar, M., Eds.), xxx
- Showman A. P., Tan X., Zhang X., 2019, *ApJ*, **883**, 4
- Showman A. P., Tan X., Parmentier V., 2020, arXiv e-prints, [p. arXiv:2007.15363](https://arxiv.org/abs/2007.15363)
- Smith K. S., Vallis G. K., 2002, *Journal of Physical Oceanography*, **32**, 1699
- Snellen I. A. G., Brandl B. R., de Kok R. J., Brogi M., Birkby J., Schwarz H., 2014, *Nature*, **509**, 63
- Steinrueck M. E., Parmentier V., Showman A. P., Lothringer J. D., Lupu R. E., 2019, *ApJ*, **880**, 14
- Stephens D. C., et al., 2009, *ApJ*, **702**, 154
- Stolker T., et al., 2020, *Astronomy & Astrophysics*, **635**, A182
- Tan X., Komacek T. D., 2019, *The Astrophysical Journal*, **886**, 26
- Tan X., Showman A. P., 2017, *ApJ*, **835**, 186
- Tan X., Showman A. P., 2019, *The Astrophysical Journal*, **874**, 111
- Tremblin P., Amundsen D. S., Chabrier G., Baraffe I., Drummond B., Hinkley S., Mourier P., Venot O., 2016, *The Astrophysical Journal Letters*, **817**, L19
- Tremblin P., et al., 2019, *The Astrophysical Journal*, **876**, 144
- Tsuji T., 2002, *ApJ*, **575**, 264

- Vallis G. K., 2006, Atmospheric and oceanic fluid dynamics: fundamentals and large-scale circulation. Cambridge University Press
- Vallis G. K., Maltrud M. E., 1993, *Journal of physical oceanography*, 23, 1346
- Vasavada A. R., Showman A. P., 2005, *Reports on Progress in Physics*, 68, 1935
- Vos J. M., Allers K. N., Biller B. A., 2017, *The Astrophysical Journal*, 842, 78
- Vos J. M., Allers K. N., Biller B. A., Liu M. C., Dupuy T. J., Gallimore J. F., Adenuga I. J., Best W. M., 2018, *Monthly Notices of the Royal Astronomical Society*, 474, 1041
- Vos J. M., et al., 2019, *Monthly Notices of the Royal Astronomical Society*, 483, 480
- Vos J. M., et al., 2020, arXiv e-prints, p. [arXiv:2005.12854](https://arxiv.org/abs/2005.12854)
- Wilson P. A., Rajan A., Patience J., 2014, *A&A*, 566, A111
- Yang H., et al., 2016, *ApJ*, 826, 8
- Zhang X., Showman A. P., 2014, *ApJ*, 788, L6
- Zhang X., Showman A. P., 2018, *The Astrophysical Journal*, 866, 1
- Zhou W., Held I. M., Garner S. T., 2014, *Journal of the Atmospheric Sciences*, 71, 1058
- Zhou Y., Apai D., Schneider G. H., Marley M. S., Showman A. P., 2016, *ApJ*, 818, 176
- Zhou Y., et al., 2018, *The Astronomical Journal*, 155, 132
- Zhou Y., Bowler B. P., Morley C. V., Apai D., Kataria T., Bryan M. L., Benneke B., 2020, arXiv e-prints, p. [arXiv:2004.05168](https://arxiv.org/abs/2004.05168)

This paper has been typeset from a \LaTeX file prepared by the author.

APPENDIX A: NUMERICAL TESTS

Figure A1 shows a test of the non-rotating 2D models with different domain length. Dominant aspects of the circulation, including the mean kinetic energy, mean cloud thickness and wind speeds are not sensitive to the chosen domain size in Figure A1. All simulations in Figure A1 exhibit characteristic large-scale structures with a size of about 2×10^4 to 4×10^4 km. Figure A2 shows the cospectral power density for $\omega'q'$ at 0.43 bar for the 2D simulations shown in Figure A1 with along an additional simulation with 48×10^4 km, demonstrating that flows with size $\sim 3 \times 10^4$ km dominate the formation and vertical transport of clouds in the non-rotating 2D systems.

APPENDIX B: DIFFERENT FORCING AMPLITUDES

Simulations shown in Figure 5 are somewhat strongly forced such that inertia gravity waves can be energetically important in the power spectra at 0.23 bar when the wavenumber is sufficiently larger than that of the deformation radius. We investigated effects of changing the forcing amplitude via adjusting the abundance of deep condensible vapor — the smaller the condensible vapor, the less forcing. In practice the settling velocity of cloud particles is artificially adjusted smaller; this is because as the circulation weakens due to the smaller forcing, it may not be able to keep cloud particles aloft to sustain the circulation. Figure B1 shows the KE power spectra for different forcing amplitudes. As the forcing becomes weaker, the transition from slope -3 to $-5/3$ gradually vanishes. In the two least forced cases, their KE power spectra exhibit a slope of -3 from the deformation radius all the way down to the scale at which KE is affected by the numerical dissipation, and no transition to $-5/3$ occurs. When the forcing is stronger, the KE power spectrum flattens out at relatively high wavenumber. Interestingly, the peak of the KE spectrum systematically moves to smaller wavenumber (larger size) as the forcing increases.

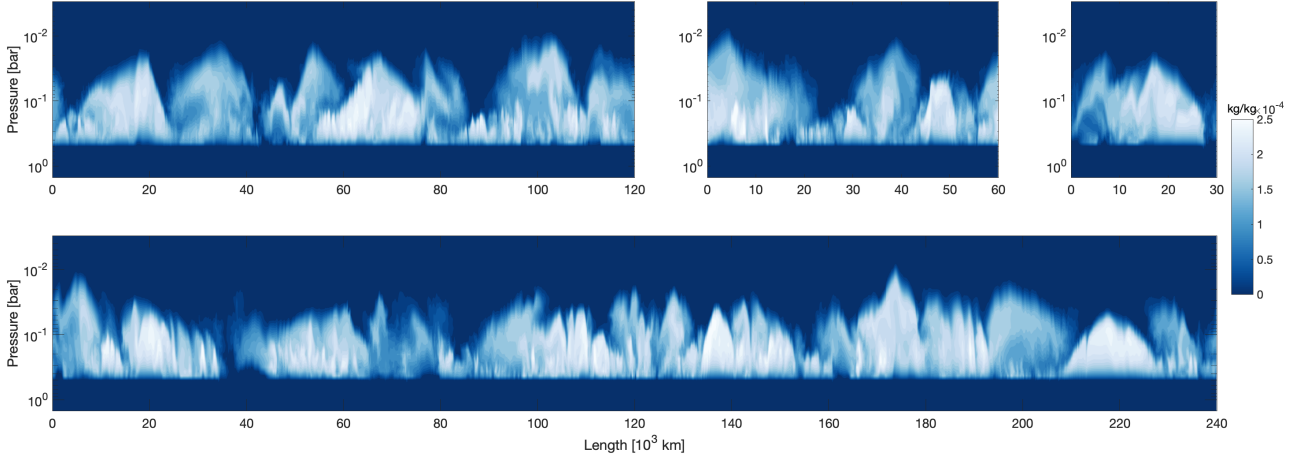


Figure A1. Instantaneous snapshots of cloud mixing ratio as a function of x and pressure for 2D simulations with different domain size of 24×10^4 , 12×10^4 , 6×10^4 and 3×10^4 km. Other model parameters, including the horizontal resolution of 150 km per grid cell, are the same among these simulations.

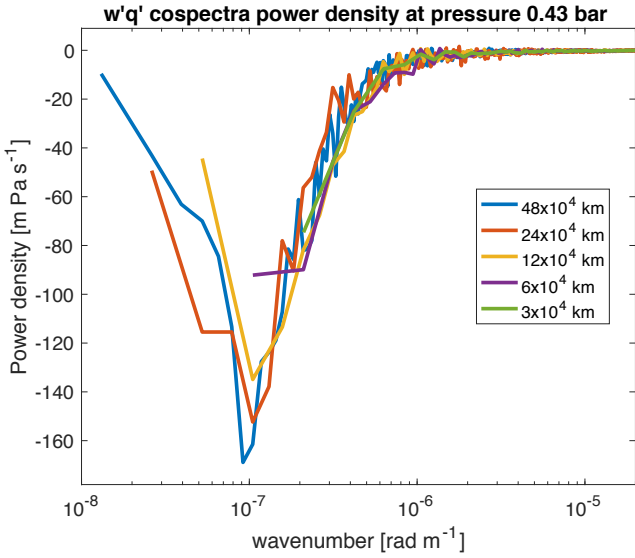


Figure A2. Cospectral power density for $\omega'q'$ at 0.43 bar for 2D simulations shown in Figure A1 with an additional one with 48×10^4 km.

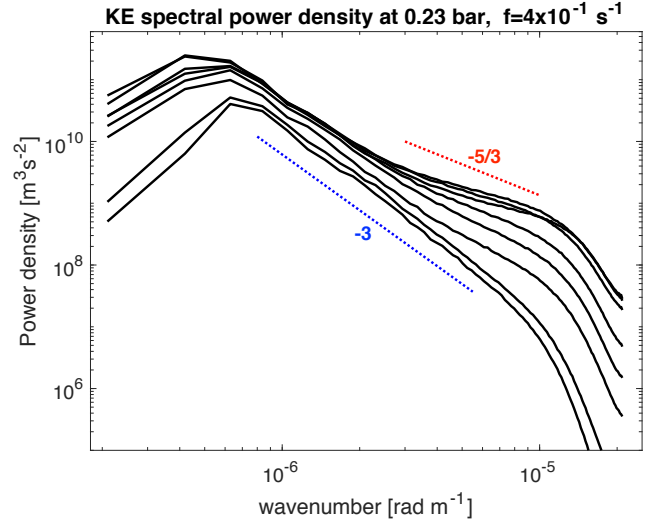


Figure B1. Kinetic energy power spectrum at a pressure of 0.23 bar from simulations with different forcing amplitudes and a Coriolis parameter $f = 4 \times 10^{-4} \text{ s}^{-1}$. The overall KE spectral power increases as the forcing amplitude increases.